The ATLAS(3D) project

Bayet, Estelle; Bureau, Martin; Davis, Timothy A.; Young, Lisa M.; Crocker, Alison F.; Alatalo, Katherine; Blitz, Leo; Bois, Maxime; Bournaud, Frederic; Cappellari, Michele

Published in:
Monthly Notices of the Royal Astronomical Society

DOI:
10.1093/mnras/sts598

Publication date:
2013

Monthly Notices
of the
ROYAL ASTRONOMICAL SOCIETY

MNRAS **432,** 1742–1767 (2013)
Advance Access publication 2013 May 11

doi:10.1093/mnras/sts598

The ATLAS^{3D} project – XVI. Physical parameters and spectral line energy distributions of the molecular gas in gas-rich early-type galaxies

Estelle Bayet,[1]⋆ Martin Bureau,[1] Timothy A. Davis,[2] Lisa M. Young,[3] Alison F. Crocker,[4] Katherine Alatalo,[5] Leo Blitz,[5] Maxime Bois,[6] Frédéric Bournaud,[7] Michele Cappellari,[1] Roger L. Davies,[1] P. T. de Zeeuw,[2,8] Pierre-Alain Duc,[7] Eric Emsellem,[2,9] Sadegh Khochfar,[10] Davor Krajnović,[2] Harald Kuntschner,[11] Richard M. McDermid,[12] Raffaella Morganti,[13,14] Thorsten Naab,[15] Tom Oosterloo,[13,14] Marc Sarzi,[16] Nicholas Scott,[17] Paolo Serra[13] and Anne-Marie Weijmans[18]†

[1]*Sub-Department of Astrophysics, Department of Physics, University of Oxford, Denys Wilkinson Building, Keble Road, Oxford OX1 3RH, UK*
[2]*European Southern Observatory, Karl-Schwarzschild-Str. 2, D-85748 Garching, Germany*
[3]*Physics Department, New Mexico Institute of Mining and Technology, Socorro, NM 87801, USA*
[4]*Department of Astronomy, University of Massachusetts, Lederle Graduate Research Tower B 619E, 710 North Pleasant Street, Amherst, MA 01003-9305, USA*
[5]*Department of Astronomy, Campbell Hall, University of California, Berkeley, CA 94720, USA*
[6]*Observatoire de Paris, LERMA and CNRS, 61 Av. de l'Observatoire, F-75014 Paris, France*
[7]*Laboratoire AIM Paris-Saclay, CEA/IRFU/SAp – CNRS – Université Paris Diderot, F-91191 Gif-sur-Yvette Cedex, France*
[8]*Sterrewacht Leiden, Leiden University, Postbus 9513, NL-2300 RA Leiden, the Netherlands*
[9]*Observatoire de Lyon, Centre de Recherche Astrophysique de Lyon and Ecole Normale Supérieure de Lyon, Université Lyon 1, 9 avenue Charles André, F-69230 Saint-Genis Laval, France*
[10]*Max-Planck Institut für extraterrestrische Physik, PO Box 1312, D-85478 Garching, Germany*
[11]*Space Telescope European Coordinating Facility, European Southern Observatory, Karl-Schwarzschild-Str. 2, D-85748 Garching, Germany*
[12]*Gemini Observatory, Northern Operations Centre, 670 N. A'ohoku Place, Hilo, HI 96720, USA*
[13]*Netherlands Institute for Radio Astronomy (ASTRON), Postbus 2, NL-7990 AA Dwingeloo, the Netherlands*
[14]*Kapteyn Astronomical Institute, University of Groningen, Postbus 800, NL-9700 AV Groningen, the Netherlands*
[15]*Max-Planck-Institut für Astrophysik, Karl-Schwarzschild-Str. 1, D-85741 Garching, Germany*
[16]*Centre for Astrophysics Research, University of Hertfordshire, Hatfield, Herts AL1 9AB, UK*
[17]*Centre for Astrophysics & Supercomputing, Swinburne University of Technology, PO Box 218, Hawthorn, VIC 3122, Australia*
[18]*Dunlap Institute, University of Toronto, 50 St George Street, Toronto, ON M5S 3H4, Canada*

Accepted 2012 December 10. Received 2012 November 20; in original form 2012 June 25

ABSTRACT

We present a detailed study of the physical properties of the molecular gas in a sample of 18 molecular gas-rich early-type galaxies (ETGs) from the ATLAS^{3D} sample. Our goal is to better understand the star formation processes occurring in those galaxies, starting here with the dense star-forming gas. We use existing integrated ^{12}CO (1–0, 2–1), ^{13}CO (1–0, 2–1), HCN (1–0) and HCO$^+$ (1–0) observations and new ^{12} CO (3–2) single-dish data. From these, we derive for the first time the average kinetic temperature, H_2 volume density and column density of the emitting gas in a significant sample of ETGs, using a non-local thermodynamical equilibrium theoretical model. Since the CO lines trace different physical conditions than of those the HCN and HCO$^+$ lines, the two sets of lines are treated separately. For most of the molecular gas-rich ETGs studied here, the CO transitions can be reproduced with kinetic temperatures of 10–20 K, H_2 volume densities of 10^{3-4} cm^{-3} and CO column densities of 10^{18-20} cm^{-2}. The physical conditions corresponding to the HCN and HCO$^+$ gas component have large uncertainties and must be considered as indicative only. We also compare for the first time the predicted CO spectral line energy distributions and gas properties of our

⋆ E-mail: bayet@physics.ox.ac.uk
† Dunlap Fellow.

molecular gas-rich ETGs with those of a sample of nearby well-studied disc galaxies. The gas excitation conditions in 13 of our 18 ETGs appear analogous to those in the centre of the Milky Way, hence the star formation activity driving these conditions is likely of a similar strength and nature. Such results have never been obtained before for ETGs and open a new window to explore further star-formation processes in the Universe. The conclusions drawn should nevertheless be considered carefully, as they are based on a limited number of observations and on a simple model. In the near future, with higher CO transition observations, it should be possible to better identify the various gas components present in ETGs, as well as more precisely determine their associated physical conditions. To achieve these goals, we show here from our theoretical study, that mid-*J* CO lines [such as the ^{12}CO (6–5) line] are particularly useful.

Key words: methods: data analysis – stars: formation – ISM: molecules – galaxies: elliptical and lenticular, cD.

1 INTRODUCTION

Early-type galaxies (ETGs) are central to our understanding of the mass assembly history of galaxies. Historically, the SAURON project[1] (de Zeeuw et al. 2002) aimed to understand the formation and evolution of elliptical galaxies, lenticular galaxies and spiral bulges from three-dimensional (3D) observations, using the panoramic optical integral-field spectrograph SAURON (Bacon et al. 2001). However, a more statistically robust sample was required to test its conclusions, and more recently the ATLAS^{3D} project[2] has targeted a complete sample of 260 ETGs within the local (42 Mpc) volume, also combining multiwavelength surveys, numerical simulations and semi-analytic modelling of galaxy formation (Cappellari et al. 2011a, hereafter Paper I). ATLAS^{3D} thus aims to constrain the dynamics of a complete volume-limited sample of ETGs, to fully characterize this class of galaxies and explore their formation and evolution.

The ATLAS^{3D} data set now provides an accurate inventory of the baryon budget of local ETGs, with a detailed two-dimensional description of the stellar and gaseous (both cold and warm) kinematics, and resolved stellar population information for all galaxies. It allows us to probe the fossil record and ask a number of specific questions. How do slow rotators form? What are the physical processes determining their kinematic and photometric properties? What is the role of major and minor mergers in their formation history? How is star formation in ETGs quenched? Is the mechanism different for fast- and slow-rotating ETGs? How does it depend on environment? And many more. Earlier ATLAS^{3D} papers have already partially addressed many of these questions (e.g. Bois et al. 2010, 2011; Cappellari et al. 2011b, hereafter Paper VII; Davis et al. 2011a, hereafter Paper X; Emsellem et al. 2011, hereafter Paper III; Khochfar et al. 2011; Krajnović et al. 2011, hereafter Paper II; Young et al. 2011, hereafter Paper IV).

ATLAS^{3D} has a built-in effort to study the cold gas in ETGs, both atomic (e.g. HI; Morganti et al. 2006; Oosterloo et al. 2010; Serra et al. 2012 and molecular (e.g. ^{12}CO; Combes, Young & Bureau 2007; Paper IV). These and other efforts in the literature (e.g. Knapp, Turner & Cunniffe 1985; Kenney & Young 1986; Knapp & Rupen 1996; Welch & Sage 2003; Sage & Welch 2006; Sage, Welch & Young 2007) have been fuelled by the realization over the past few decades that many ETGs, previously thought to be 'red and dead', actually harbour a substantial amount of cold (hence molecular) gas, and that many have a non-negligible level of star formation (e.g. Welch & Sage 2003; Combes et al. 2007; Crocker et al. 2011).

More chemically complex species such as HCO^+ and HCN as well as the less abundant isotopomer ^{13}CO have also recently been observed in ATLAS^{3D} ETGs (Krips et al. 2010; Crocker et al. 2012, hereafter Paper XI), mostly using single-dish telescopes. Paper XI presents IRAM 30 m telescope observations of the 18 ^{12}CO-brightest ATLAS^{3D} ETGs in the ^{13}CO (1–0), ^{13}CO (2–1), HCN (1–0) and HCO^+ (1–0) lines. Several key molecular line ratios are investigated as empirical indicators of the molecular gas physical conditions. Comparison with spiral galaxies shows that the line ratios of ETGs and spirals generally overlap, but many ETG outliers also exist. A few ETGs have more starburst-like line ratios, while a few others have very low ^{12}CO/^{13}CO ratios. Correlations of line ratios involving ^{12}CO (1–0) are found with many galaxy properties: molecular-to-atomic gas mass fraction, dust temperature, dust morphology and stellar population age. Overall, it seems as if the driver of these correlations is a reduced optical depth in ETGs that have recently acquired or are in the process of acquiring their cold gas.

While these results are suggestive, Paper XI does not include modelling of the line ratios to derive the physical conditions of the molecular gas. Detailed modelling has been performed for only one ETG to date, Centaurus A (Ebneter & Balick 1983; Eckart et al. 1990; Liszt 2001), with several molecular absorption lines observed towards its nucleus (e.g. Eckart et al. 1990; Wild, Eckart & Wiklind 1997; Muller & Dinh-V-Trung 2009). No systematic and homogenous study, based on a comparison of observations of a well-defined sample of ETGs with theoretical models, has ever been performed. To better understand the evolution of the cold gas and associated star formation in ETGs, it is however essential to constrain gas physical parameters such as the kinetic temperature, H_2 volume density and the column density of species such as CO, HCN and HCO^+, even if they are averaged over entire galaxies.

Here, we therefore aim to estimate the globally averaged physical properties of the molecular gas in a significant sample of ETGs (18), using a single-dish data set (largely the observations presented in Paper XI) and focusing on the two gas components traced by the CO and HCN/HCO^+ lines, respectively. As this first study is by necessity exploratory, we use a simple theoretical framework, non-local thermodynamical equilibrium (non-LTE) model, specifically the Large Velocity Gradient (LVG) model developed by van der Tak et al. (2007). We have also recently obtained ^{12}CO (3–2) observations with the HARP instrument on the James Clerk Maxwell

[1] http://www.strw.leidenuniv.nl/sauron/
[2] http://www-astro.physics.ox.ac.uk/atlas3d/

Telescope (JCMT) for a few objects. We report both on these new observations and the theoretical model in this paper.

The structure of the paper is as follows. We first present new CO (3–2) observations of eight sample galaxies with existing multiline observations in Section 2, and briefly review the main characteristics of the other observations on which our theoretical analysis is based. The main assumptions and parameters of the LVG model are described in Section 3. The comparison of the model predictions and observations, and the identification of the models reproducing best the data are detailed in Section 4. A discussion of our results and literature data are then presented in Section 5. The results are discussed further in Section 6 where we also conclude briefly. We remind the reader that all the basic properties of our sample galaxies can be found in previous ATLAS^{3D} papers (e.g. Paper I).

2 OBSERVATIONS

2.1 Literature data

Most of the ^{12}CO, ^{13}CO, HCN and HCO$^+$ molecular gas detections in ETGs that we are using here for modelling are taken from previously published SAURON and ATLAS^{3D} follow-ups. Observational parameters beyond those detailed below can be found in these studies (Welch & Sage 2003; Combes et al. 2007; Krips et al. 2010; Paper IV; Paper XI). To be more precise, observations of the HCN (1–0) ($\nu = 89.087$ GHz), HCO$^+$ (1–0) ($\nu = 89.188$ GHz), ^{13}CO (1–0) ($\nu = 110.201$ GHz) and ^{13}CO (2–1) ($\nu = 220.398$ GHz) lines were presented in Krips et al. (2010) and Paper XI, following-up on the 18 strongest ^{12}CO (1–0) ($\nu = 115.271$ GHz) and ^{12}CO (2–1) ($\nu = 230.538$ GHz) detections of Combes et al. (2007) and Paper IV.

2.2 New ^{12}CO (3–2) observations

New ^{12}CO (3–2) ($\nu = 345.795$ GHz) observations of 8 of those 18 galaxies were acquired at the JCMT (project m11au11) between 2011 March 31 and September 4. These galaxies are pathfinders for a larger ^{12}CO (3–2) survey, and were selected because of their bright ^{12}CO (1–0) fluxes. For five galaxies (IC 0676, IC 1024, NGC 6014, PGC 058114 and UGC 09519), the HARP receiver and ACSIS backend were used in a configuration yielding a 1 GHz total bandwidth and 2048 channels each 488 kHz wide. Three galaxies (NGC 3665, NGC 4526 and NGC 5866) have broader lines (see Fig. 1) and for those the backend configuration used two overlapping sub-bands, each 1 GHz wide and covering a total bandwidth of 1.9 GHz with 977 kHz-wide channels. Observations were carried out in the grid-chop or staring mode, with beam switching and a 90 arcsec throw. Opacities at 225 GHz (τ_{225}) ranged from 0.05 to 0.1 and system temperatures (at 345 GHz) from 230 to 370 K. Pointing tests before each galaxy observation and less-frequent focus calibrations were made on the standard sources RXBoo, IRC+10216, IRC+20326, CIT6, RTVir and XHer, and the average pointing offset was 3–4 arcsec. Repeated observations of the standard sources G34.3 and 16293−2422 every night suggest that the absolute calibration is constant at the 2–5 per cent level. Stable baselines required only a zeroth-order baseline subtraction. Conversion from antenna temperature to main beam brightness temperature was done via $T_{\rm mb} = T_{\rm A}^*/0.6$ (see Warren et al. 2010 or the references in http://www.jach.hawaii.edu/JCMT/spectral_line/ and http://www.jach.hawaii.edu/JCMT/spectral_line/Standards/current_cals.html). The half-power beam width of the JCMT at $\nu \approx 345$ GHz is 14 arcsec.

The data pre-reduction for the new ^{12}CO (3–2) observations was done using Starlink software (KAPPA, SMURF and STLCONVERT packages[3]), and the data were subsequently translated to CLASS[4] format for final reduction. The reduced spectra for all eight galaxies are presented in Fig. 1 and the integrated intensities are listed in Table 1. No other CO (3–2) observation is available so far. The ^{12}CO (3–2) line profile in NGC 4526 is asymmetric, probably caused by a combination of a small pointing error and the emission region being slightly larger than the beam at this frequency (causing some 'missing' flux at low velocities). With only single-dish information, it is difficult to precisely estimate how much flux is missed. However, we do have recently acquired interferometric ^{12}CO (2 1) CARMA data of NGC 4526 (Davis et al., in preparation), and estimate ≈8 per cent of missing flux. We have checked that our conclusions remain unchanged when using the corrected flux (see Section 4). The ^{12}CO (3–2) line emission of IC 1024 suffers from a greater pointing uncertainty that does not allow us to use this detection in our modelling work (Section 3). Observations of IC 1024 alone used the jiggle-chop mode with a 4 × 4 map-centred grid, yielding a square grid of spectra spaced by 7.5 arcsec. The optical centre of the galaxy therefore does not fall on a grid position, and we averaged the four central spectra to produce the spectrum shown in Fig. 1. The resulting averaged line profile is however significantly different from those of the ^{12}CO (1–0) and ^{12}CO (2–1) lines (see Paper XI), with a peak flux velocity more than 100 km s^{-1} away from those of the lower J CO lines and a ^{12}CO (3–2) line width 20 per cent smaller. Any ^{12}CO (3–2) flux correction would thus be highly uncertain, and we do not include this detection in our modelling work. Overall, we therefore have reliable ^{12}CO (3–2) observations for 7 of our 18 sample galaxies.

2.3 Data reduction and analysis

The data reduction for all galaxies, including the ^{12}CO (3–2) line, has been performed (or redone when already published) in a systematic and homogeneous way using the GILDAS package, as described in Paper XI. As the line profiles are not always Gaussian, velocity-integrated line intensities were extracted by simply summing the intensities over the range of velocities with detected ^{12}CO (1–0) emission (see Paper IV). Although the ^{12}CO (3–2) emission of NGC 6014 and PGC 058114 is slightly off-centred within that range, we have kept it for consistency with previously published results. The statistical uncertainties resulting from this method are discussed in great detail in Paper XI and lead to errors on the velocity-integrated line intensities of ≤10 per cent. If the peak flux is lower than three times the rms noise in line-free channels (integrated over the expected velocity range), as is the case for several galaxies in the HCN (1–0) and HCO$^+$ (1–0) lines, the line is considered undetected and an upper limit of three times the rms noise is adopted.

The LVG models (see Section 3.2) also require the observed line widths of each transition and molecule. Depending on the source and spectrum, we use either a Gaussian or a double-peaked line profile fit to extract the line width, taking the line width as the full-width at half-maximum (FWHM) for Gaussian profiles and the velocity width given by the shell method for double-peaked profiles.[5] These

[3] See http://www.jach.hawaii.edu/JCMT/spectral_line/data_reduction/acsisdr/basics.html.

[4] See http://www.iram.fr/IRAMFR/GILDAS/doc/html/class-html/class.html.

[5] More details are available in the GILDAS package for both methods.

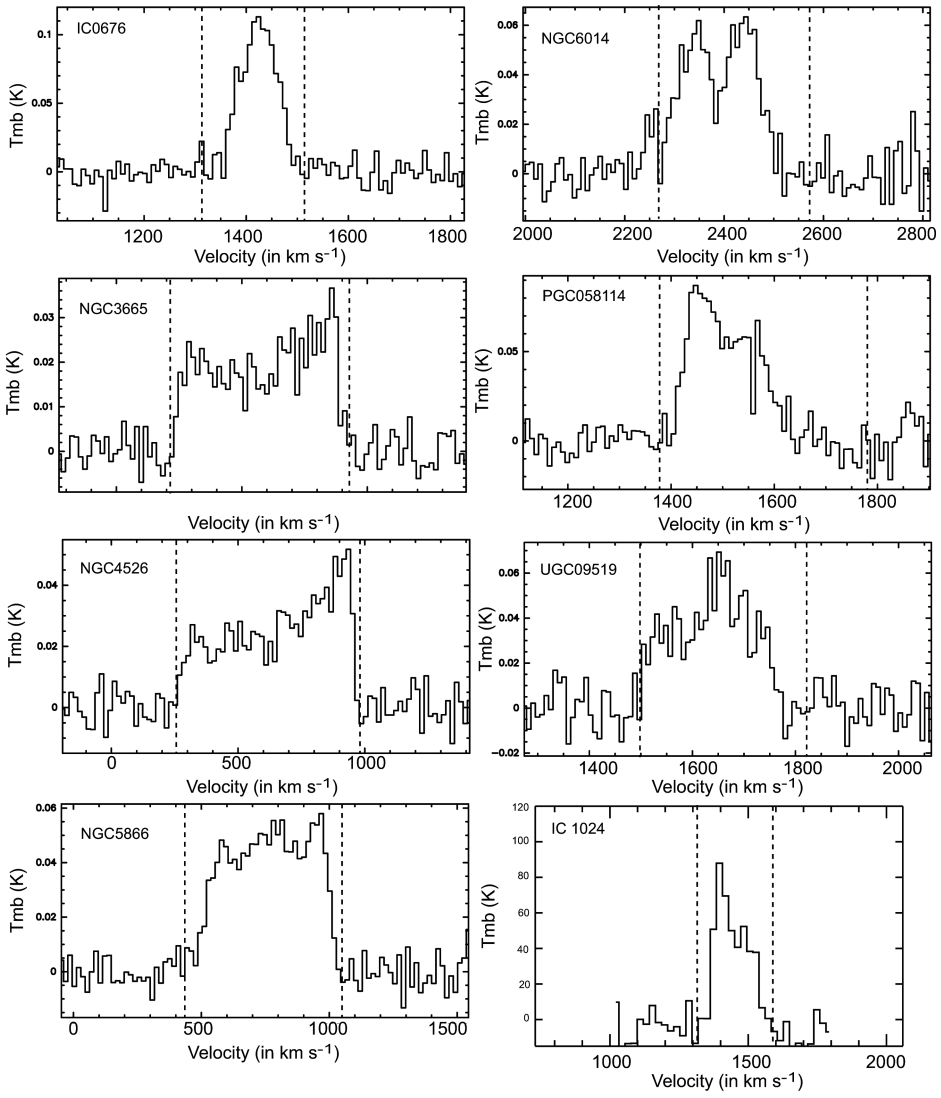

Figure 1. New JCMT ^{12}CO (3–2) line observations of eight galaxies from our sample. As the line profiles are not always Gaussian, velocity-integrated line intensities were extracted by simply summing the intensities over the range of velocities (indicated by the dashed lines) with detected ^{12}CO (1–0) emission (see Paper IV). Although IC 1024 is clearly detected in ^{12}CO (3–2), both the shape and scaling of its line profile are highly uncertain due to a pointing error. We thus present the IC 1024 data here for completeness only.

Table 1. Velocity-integrated line intensities of the new ^{12}CO (3–2) JCMT data (see Section 2).

Galaxy	$\int T_{\rm mb}\,\Delta v$ (K km s^{-1})
IC 0676	10.14 ± 0.34
IC 1024	9.57 ± 0.74
NGC 3665	12.32 ± 0.41
NGC 4526	18.58 ± 0.58
NGC 5866	23.84 ± 0.59
NGC 6014	8.60 ± 0.46
PGC 058114	9.01 ± 0.47
UGC 09519	11.93 ± 0.52

provide satisfactory estimates given the crude model assumptions. The line widths are tabulated in Table 2, where the errors reported are formal fitting uncertainties, with an average of 20 per cent. For undetected lines (flux upper limits), we take a line width equal to that of the 'closest' molecular species. For example, when undetected, we have assumed that HCO^+ (1–0) has the same line width as the HCN (1–0), since we consider that both species trace the same gas component. Similarly, when the ^{12}CO (2–1) or ^{13}CO (2–1) transitions only have upper limits, their line widths are assumed to be the same as those of the ^{12}CO (1–0) and ^{13}CO (1–0) transitions, respectively. When both HCN and HCO^+ are undetected, we have not attempted to calculate the corresponding line ratio nor to identify any best model, as the ratio of two upper limits is unconstrained. For those cases, we do not provide any line width either (see Table 2).

3 NON-LTE MODELS

3.1 Generalities

As shown theoretically (e.g. Spaans & Meijerink 2005; Meijerink, Spaans & Israel 2007; Bayet et al. 2008b, 2009b) and confirmed

Table 2. Line widths for our sample of 18 gas-rich ETGs, extracted from the observations published in Paper XI and from the new ^{12}CO (3–2) observations presented here.

Galaxy	D (Mpc)	Δv (^{12}CO (1–0)) (km s^{-1})	Δv (^{12} CO(2–1)) (km s^{-1})	Δv (^{12}CO (3–2)) (km s^{-1})	Δv (^{13}CO (1–0)) (km s^{-1})	Δv (^{13}CO (2–1)) (km s^{-1})	Δv (HCN (1-0)) (km s^{-1})	Δv (HCO$^+$(1–0)) (km s^{-1})
IC 0676	24.6	97.3 ± 17.4	87.1 ± 10.7	84.1 ± 3.1	150.2 ± 39.1	77.7 ± 16.1	101.2 ± 28.1	116.8 ± 26.7
IC 1024	24.2	160.9 ± 19.3	146.9 ± 22.4	123.1 ± 20.0	191.0 ± 30.6	152.6 ± 19.8	–	–
NGC 1222	33.3	158.7 ± 10.4	169.8 ± 15.7	–	170.8 ± 31.8	133.7 ± 17.7	–	128.7 ± 30.0
NGC 1266	29.9	128.1 ± 22.3	152.2 ± 28.9	–	95.1 ± 19.1	104.0 ± 20.5	157.3 ± 48.3	179.6 ± 13.7
NGC 2764	39.6	249.5 ± 6.6	226.0 ± 7.0	–	250.9 ± 22.8	246.3 ± 25.0	220.3 ± 62.4	199.2 ± 34.6
NGC 3032	21.4	128.8 ± 14.5	102.5 ± 3.3	–	80.8 ± 16.5	103.4 ± 11.2	162.5 ± 45.5	–
NGC 3607	22.2	268.6 ± 40.5	323.1 ± 4.7	–	425.9 ± 85.2	386.7 ± 68.6	385.4 ± 71.4	387.3 ± 77.8
NGC 3665	33.1	318.1 ± 64.7	319.4 ± 51.7	317.8 ± 54.7	327.5 ± 65.5	312.6 ± 76.8	318.3 ± 27.8	–
NGC 4150	13.4	159.2 ± 13.8	189.1 ± 17.6	–	149.0 ± 29.8	158.2 ± 30.4	–	–
NGC 4459	16.1	194.6 ± 35.7	192.7 ± 28.9	–	196.3 ± 33.3	190.1 ± 39.3	193.3 ± 42.5	–
NGC 4526	16.4	348.9 ± 34.9	341.1 ± 68.0	336.7 ± 53.8	345.6 ± 55.3	345.2 ± 72.5	346.7 ± 73.4	–
NGC 4694	16.5	80.2 ± 5.2	70.9 ± 14.2	–	57.9 ± 9.3	100.8 ± 30.3	–	–
NGC 4710	16.5	229.2 ± 45.3	209.5 ± 42.0	–	292.7 ± 52.8	261.8 ± 52.1	243.0 ± 59.5	272.5 ± 43.4
NGC 5866	14.9	294.8 ± 50.5	242.5 ± 48.6	240.7 ± 43.3	374.3 ± 71.1	377.9 ± 74.1	338.6 ± 71.9	360.5 ± 33.6
NGC 6014	35.8	179.7 ± 28.8	122.1 ± 24.6	107.2 ± 14.0	162.1 ± 25.9	140.8 ± 29.5	93.3 ± 17.9	–
NGC 7465	29.3	129.8 ± 24.8	80.1 ± 12.7	–	140.8 ± 19.7	130.9 ± 27.6	150.5 ± 42.6	124.7 ± 12.9
PGC 058114	23.8	155.8 ± 29.6	160.5 ± 32.1	149.4 ± 22.4	174.9 ± 27.9	154.7 ± 32.5	–	170.9 ± 54.4
UGC 09519	27.6	179.5 ± 32.1	155.0 ± 31.5	128.0 ± 15.7	153.1 ± 26.0	199.5 ± 46.9	–	141.2 ± 34.2

Note. The symbol '–' implies that no line width could be measured, either because there is no observation [e.g. ^{12}CO(3–2) line] or because signal-to-noise ratio of the line is too low. However, when required, the line width adopted is that from the 'closest' species (see Section 2).

observationally (e.g. Israel & Baas 2003; Gao & Solomon 2004; Kramer et al. 2005; García-Burillo et al. 2006; Bayet et al. 2008a, 2009a; Aladro et al. 2011), there are several distinct cold gas components in external galaxies, each traced by specific molecular tracers. For our modelling, we thus consider a simple approach with two gas components: one traced by the CO lines (a rather extended and cool phase) and another traced by the HCN and HCO$^+$ lines (expected to be warmer and denser). This approach is most appropriate given the significant differences between the critical line densities of these species, i.e. more than two orders of magnitude between HCO$^+$ (1–0) and ^{12}CO (1–0), and three orders of magnitude between HCN (1–0) and ^{12}CO (1–0). The gas traced by the low-J CO lines and the gas traced by HCO$^+$ and HCN are thus not compatible; mixing these two components would not allow us to increase our knowledge of the interstellar medium (ISM) properties of ETGs as much as the two-component approach adopted. We do note that HCN (1–0) and HCO$^+$ (1–0) do not have exactly the same critical line density (approximately one order of magnitude difference), and thus they do not strictly speaking trace the same gas component. However, in the rest of the current paper we will consider that they do, in the sense that they both qualitatively trace a gas component denser than that observed with the low-J CO lines.

In the following, we refrain to estimate gas masses and gas fractions, as there are large uncertainties in the values of the appropriate conversion factors for ETGs (CO-to-H_2 and HCN-to-H_2). In fact, there is currently no estimate of the HCO$^+$-to-H_2 conversion factor at all in the literature, even for late-type galaxies, so it is clearly not possible to estimate the gas mass and gas fraction associated with this species. Nevertheless, qualitative empirical estimates of gas fractions based on the line ratios of ^{12}CO, ^{13}CO, HCN and HCO$^+$ were discussed in Paper XI.

3.2 Model description

To determine the average physical properties of the CO gas component on the one hand, and those of the HCN and HCO$^+$ gas component on the other hand, we use RADEX, the non-LTE model developed by van der Tak et al. (2007). This model is a zero-dimensional, one molecular species code. It solves the radiative transfer equations by assuming a homogeneous medium and retaining the assumption of local excitation. To partially decouple the level population and radiative transfer equations, the van der Tak et al. (2007) model uses the escape probability method (one variation of which is the LVG method) assuming a uniform (i.e. non-expanding) sphere. The escape probability equation is then given by Osterbrock (1974). The model also assumes that the optical depth is independent of velocity, appropriate for modelling velocity-integrated line intensities.

Although the assumption of uniform physical conditions for each gas component over the scale of a galaxy is crude (e.g. the ISM of nearby galaxies is known to be clumpy), these models do provide first-order constraints on the average physical conditions, and they do represent a useful first step in predicting the intensities of the higher order transitions of CO, HCN and HCO$^+$, on which there is currently no constraint in ETGs. In any case, we currently lack information on the very small scale (<70 pc) gas distribution of ETGs, preventing us from studying their gas properties in greater detail.

Molecular collisional rates are required to derive the molecular gas physical conditions using this model, in addition to the spectroscopic and dipole moment data (Müller et al. 2001, 2005)[6] needed when using more basic (e.g. LTE) models. We used collisional rates for CO, HCN and HCO$^+$ from the Leiden Atomic and Molecular Database (LAMBDA) (Schöier et al. 2005)[7] as recommended in van der Tak et al. (2007).

There are five main parameters in the LVG model we use: the column density $N(X)$ of the species studied X (here either ^{12}CO, ^{13}CO, HCN or HCO$^+$) in cm^{-2}, the line width Δv of each transition (see Table 2) in km s^{-1}, the molecular hydrogen volume density

[6] From The Cologne Database for Molecular Spectroscopy (CDMS); see http://www.astro.uni-koeln.de/cdms/

[7] http://www.strw.leidenuniv.nl/~moldata/

$n(H_2)$ in cm^{-3}, the kinetic temperature T_K in K and the abundance ratios (e.g. isotopic ratios such as $^{12}C/^{13}C$ and the HCN/HCO^+ abundance ratio). In our work, we leave the three parameters T_K, $n(H_2)$ and $N(X)$ free (and solve for them by fitting the data), whereas we fix the other parameters (Δv and isotopic abundance ratios). We note that we do not implement more specific characteristics of ETGs in our LVG models, such as high metallicity or enhanced α-element abundances. These particularities and their detailed influence on the molecular chemistry of ETGs have however been considered in Bayet et al. (2012).

3.3 Choice of parameters

As discussed above (Section 2.3), the fixed parameter Δv is taken as the FWHM of the fit for Gaussian profiles or the line width of the fit for double-peaked profiles, and is measured for each molecular line in each source (see Table 2). It varies from 58 to 425 km s^{-1}, and its value directly impacts on the predicted velocity-integrated line intensity calculated by the LVG model. Indeed, the predicted velocity-integrated intensities are obtained by multiplying the calculated radiation temperature of the spectral line by $1.06\,\Delta v$, where the factor 1.06 is due to the assumption of a Gaussian line profile. Although not all line profiles are Gaussian, the models are constrained only by ratios of velocity-integrated line intensities, so this factor and the assumed shape of the line profiles have no influence on the model fits; only variations in the line profiles across the different lines involved in the ratios matter. This is no longer true for the calculation of the predicted spectral line energy distributions (SLEDs), however, and the SLEDs of galaxies with non-Gaussian line profiles are therefore more uncertain (see Section 4.3).

Currently, there is little knowledge of the true isotopic abundance ratio of carbon in ETGs and of its variation from source to source. We have thus assumed that it is constant across our sample. As explained for instance by Martín et al. (2010) and Roberts et al. (2011), velocity-integrated line intensity ratios can be misleading and are not a good proxy for abundance ratios, as they are affected by geometry and optical depth effects. The velocity-integrated line intensity ratios of $^{12}CO/^{13}CO$ provided in Paper XI (see their fig. 3) cannot therefore be used to derive an accurate value of the intrinsic $^{12}C/^{13}C$ abundance ratio. Similarly for HCN (1–0)/HCO^+ (1–0), Wilson & Rood (1994) reported values of the $^{12}C/^{13}C$ abundance ratio in the centre of the Milky Way, the 4 kpc molecular ring, the local ISM and the Solar system of $\approx$20, 50, 70 and 90, respectively. For local starburst galaxies, it has been recently estimated to be $>$46 (Martín et al. 2010). Based on optically thin lines, Roberts et al. (2011) reported an HCN/HCO^+ abundance ratio between 0.5 and 1.03 for local and extragalactic active star-forming regions. For the Galactic Centre, only optically thick lines of HCN and HCO^+ are present in the literature (and are thus misleading). Lacking better information for either case, we have therefore adopted a fixed value of 70 for the $^{12}C/^{13}C$ abundance ratio and a value of 1 for HCN/HCO^+. Only knowledge of the small-scale distribution of the ^{12}CO, ^{13}CO, HCN and HCO^+ emission for various line transitions would allow us to properly estimate the true abundance ratios.

We thus built four grids of LVG models to be combined, one for each of ^{12}CO, ^{13}CO, HCN and HCO^+. Each grid covers kinetic temperatures of 10–250 K in steps of 10 K, gas volume densities of 10^3–10^7 cm^{-3} in steps of 0.5 dex, column densities of 10^{10}–10^{20} cm^{-2} in steps of 0.5 dex and line widths of 60–430 km s^{-1} in steps of 10 km s^{-1}. Each grid thus contains over 150 000 models, leading to a total of over 600 000 models for the species investigated in this study.

The model outputs are numerous, and among them is the quantity we are primarily interested in, i.e. the predicted velocity-integrated line intensity (in K km s^{-1}). We ran each model to include the first 15 energy levels and therefore the first 15 transitions of each species, allowing us to predict the most interesting observational lines for *Herschel* Observatory and the Atacama Large Millimeter/submillimeter Array (ALMA) (see Section 4.3).

For each galaxy, we have thus compared the predicted velocity-integrated line intensity ratios (computed directly from the model outputs) with the observed ones. More specifically, we have worked with the independent ^{12}CO (1–0)/^{13}CO (1–0), ^{12}CO (2–1)/^{13}CO (2–1), ^{12}CO (1–0)/^{12}CO (2–1) and ^{12}CO (1–0)/^{12}CO (3–2) (whenever the ^{12}CO (3–2) line was available; see Table 1) line ratios on the one hand, and the HCN (1–0)/HCO^+ (1–0) line ratio on the other hand. For each ratio, we have corrected for beam dilution as described in Paper XI. The ^{12}CO (3–2) line emission is only used in one ratio, not two, because we wanted to keep independent constraints for reliable χ^2 calculations (see Section 4.2).

To identify the model whose input parameters [T_K, $n(H_2)$ and $N(X)$] reproduce best the observed line ratios, we have therefore constrained the models with a minimum of three observed line ratios for the CO gas component, and only one observed line ratio for the HCN and HCO^+ gas component. The physical properties derived for the CO gas component are thus more reliable than those derived for the HCN and HCO^+ one, as the latter are underconstrained. The results for the HCN and HCO^+ gas component should therefore be considered purely as indicative, and we present these results (table and figures) in Appendix A only. We will focus exclusively on the CO gas component for the remainder of the current paper.

Finally, we note that the observed line ratios involving isotopologues [^{12}CO (1–0)/^{13}CO (1–0) and ^{12}CO (2–1)/^{13}CO (2–1)] have been reproduced by combining a ^{12}CO model having a column density $N(^{12}CO)$ with a ^{13}CO model having a column density $N(^{13}CO) = (^{13}C/^{12}C)N(^{12}CO)$. Similarly, an observed ratio line involving a ^{12}CO (1–0) line with an FWHM of 300 km s^{-1} and a ^{12}CO (2–1) line with an FWHM of 290 km s^{-1} has been reproduced by combining a ^{12}CO model having a velocity width of 300 km s^{-1} for the (1–0) transition with a ^{12}CO model having a velocity width of 290 km s^{-1} for the (2–1) transition.

4 RESULTS

We explore below two complementary methods to identify the 'best' model for each galaxy studied: the best-fitting model based on the χ^2 method (see Section 4.1) and the most likely model based on the likelihood (see Section 4.2). From these two methods, we calculate for the first time the corresponding predicted SLEDs of CO in local ETGs (see Section 4.3).

4.1 Best-fitting model identification

For each source, we identify a best model using the χ^2 minimization method for each of the two gas components investigated, i.e. the gas traced by CO on the one hand and the gas traced by HCN and HCO^+ on the other. The physical properties [T_K, $n(H_2)$ and $N(X)$] corresponding to these best fits are listed, respectively, in Table 3 for the CO gas component and in Table A1 for the HCN and HCO^+ component. This is the first time that the physical properties of the molecular gas are constrained in ETGs in a systematic and homogeneous way, and for a relatively large number of sources (18). These properties are of prime interest for further individual and statistical studies of the gas in ETGs (physical conditions, origin,

Table 3. Best-fitting model parameters of the CO gas component.

Galaxy	χ^2	T_K (K)	$n(H_2)$ (cm^{-3})	$N(CO)$ (cm^{-2})
IC 0676[a]	1.07	70	10^3	$10^{19.5}$
IC 1024	0.56	20	10^4	10^{19}
NGC 1222	2.06	20	$10^{6.5}$	10^{19}
NGC 1266	0.85	20	10^4	$10^{18.5}$
NGC 2764	0.11	10	$10^{3.5}$	10^{19}
NGC 3032	5.32	10	$10^{3.5}$	10^{19}
NGC 3607	0.23	50	10^3	10^{20}
NGC 3665[a]	6.45	10	$10^{3.5}$	10^{20}
NGC 4150	0.02	20	$10^{3.5}$	10^{19}
NGC 4459	0.57	10	10^4	$10^{19.5}$
NGC 4526[a]	1.28	20	$10^{3.5}$	10^{20}
NGC 4694	2.15	10	$10^{3.5}$	$10^{18.5}$
NGC 4710	1.38	20	$10^{3.5}$	$10^{19.5}$
NGC 5866[a]	41.18	10	10^7	$10^{19.5}$
NGC 6014[a]	1.45	120	10^3	10^{20}
NGC 7465	9.95	150	$10^{4.5}$	10^{20}
PGC 058114[a]	0.34	30	$10^{3.5}$	10^{19}
UGC 09519[a]	25.21	40	10^3	10^{19}

[a]Galaxies with a ^{12}CO (3–2) line flux used in the modelling work.

HI-to-H_2 ratio, etc). When calculating the χ^2, the errors on the observed line ratios have been properly calculated and are fully taken into account. As the errors on line ratios are asymmetric (see Paper XI), we have considered the geometric average of the two values in our χ^2 calculations.

The kinetic temperatures obtained for the best-fitting models are either low (T_K = 10–20 K for IC 1024, NGC 1222, NGC 1266, NGC 2764, NGC 3032, NGC 3665, NGC 4150, NGC 4459, NGC 4526, NGC 4694, NGC 4710 and NGC 5866), intermediate (30–70 K for IC 0676, NGC 3607, PGC 058114 and UGC 09519) or high (120 K for NGC 6014 and 150 K for NGC 7465). Although these kinematic temperatures may seem high in view of the commonly assumed low star-formation activity of ETGs, the fact is that the absolute star formation rates (SFRs) of ETGs are not always low (especially in the molecular gas-rich objects considered here). It is the specific SFRs (SSFRs; i.e. the SFRs per unit stellar mass) that are generally lower than those of spirals (see, e.g., Shapiro et al. 2010 for the SAURON ETGs). ETGs also have additional heating, excitation and ionization mechanisms that are unlikely to be important in other galaxy types. For example, old (and therefore not massive) but hot stars will heat the dust grains and, through the photoelectric effect, the gas, impacting both the molecular and ionized gas emission lines. This peculiar population also gives rise to the ultraviolet (UV)-upturn phenomenon (e.g. O'Connell 1999; Bureau et al. 2011; Jeong et al. 2012), increasing the UV flux (and thus the heating) surrounding the gas independently of star formation. Supernova rates leading to cosmic ray fluxes may also be different than those of spirals. Finally, the high stellar metallicity and α-element enhancement may also play a role in the gas chemistry (Bayet et al. 2012). Any or all of these mechanisms may thus partly be responsible for the high gas temperatures measured in some galaxies, although it is impossible at this point to determine which has the greatest influence.

The best-fitting H_2 volume densities do not vary by more than a factor of 10 between our sources [$n(H_2) = 10^{3-4}\,cm^{-3}$], except for NGC 1222 and NGC 5866 that have $n(H_2) = 10^{6.5}$ and $10^7\,cm^{-3}$, respectively. Similarly, the CO column densities derived are pretty constant amongst all the galaxies studied, with $N(CO) = 10^{18.5-20}\,cm^{-2}$. These column densities may appear high, especially once converted to $N(H_2)$. Indeed, assuming a standard Milky Way CO-to-H_2 abundance ratio of 10^{-4}, one obtains $N(H_2) = 10^{22.5-24}\,cm^{-2}$, corresponding to an average surface mass density of $10^{2.5-4}\,M_\odot\,pc^{-2}$. For comparison, giant molecular clouds in the Milky Way have typical surface densities of $10^2\,M_\odot\,pc^{-2}$. However, as shown by Bayet et al. (2012) who studied in details the chemistry of ETG-like environments, the standard Milky Way CO/H_2 fractional abundance is not appropriate for ETGs, and a value higher than 10^{-4} should be used (see fig. 2 in Bayet et al. 2012). For most of the sources studied here, a value of $10^{-2.5}$ is more appropriate, leading to surface densities closer to the Milky Way value. In addition, high CO column densities may not be totally unexpected, as suggested by our CO interferometric maps (Alatalo et al. 2013, hereafter Paper XVIII), where high surface densities are observed despite low SSFRs (as high as $\approx 10^4\,M_\odot\,pc^{-2}$ in NGC 1266). These CO column densities may also be considered as lower limits, since the authors conservatively assumed a standard CO-to-H_2 conversion factor. This apparent low star formation efficiency (i.e. the SFR per unit dense gas mass) may partly be due to the different dynamics of ETGs compared to that of spirals (morphological quenching; see Martig et al. 2009). Nevertheless, most ETGs show typical surface densities of $\approx 10^2\,M_\odot\,pc^{-22}$, consistent with Milky Way values.

Table 3 reveals that the galaxies detected in ^{12}CO (3–2) are not systematically those showing the highest kinetic temperatures and gas densities as determined by the best-fitting method (see, e.g., NGC 3665 and NGC 4526). As it takes warmer and denser gas to effectively populate the (3–2) level, this may seem surprising at first, but in fact our best-fitting results only show that the ^{12}CO (3–2) line in these galaxies is not the main driver of our best-fitting model identification. In other words, there is basically nothing special about the objects detected in ^{12}CO (3–2). In fact, we did not select for observations objects predicted to have the highest absolute ^{12}CO (3–2) fluxes, but rather the highest *apparent* ^{12}CO (3–2) fluxes [e.g. because they are nearby or have high ^{12}CO (1–0) fluxes]. So the other objects are not so much non-detections as they are non-observations [we just do not know what their ^{12}CO (3–2) fluxes are, and they may well be high]. A larger sample of ^{12}CO (3–2) observations in ETGs is thus needed for further comparison.

Understanding the exact driver of the best-fitting model identification requires a detailed analysis of the LVG code outputs and of the χ^2 minimization that are outside the scope of this paper. However, to evaluate the accuracy of our best-fitting CO models and calculate uncertainties on the derived best-fitting model parameters listed in Table 3, we have calculated the $\Delta\chi^2 \equiv \chi^2 - \chi^2_{min}$ contours for each source in our 3D parameter space [T_K, $n(H_2)$, $N(CO)$]. The first five contours in Fig. 2 show the 1–5σ [8] confidence level contours in three T_K–$n(H_2)$ planes centred on the best-fitting $N(CO)$ value, where dark grey dots (red dots in the online version) correspond to individual models. The $\Delta\chi^2$ contours for the HCN and HCO^+ gas component are presented in Fig. A1. Additional contours of $\Delta\chi^2$ = 50, 100, 200 and 300 are used in these figures only for guiding the eyes further and see better how the confidence contours are spreading within the model grid.

With additional (higher J levels) observations of the same species, probing denser and warmer gas closer to the forming stars, we should be able to (i) confirm the results obtained here and

[8] The σ symbol represents the standard deviation.

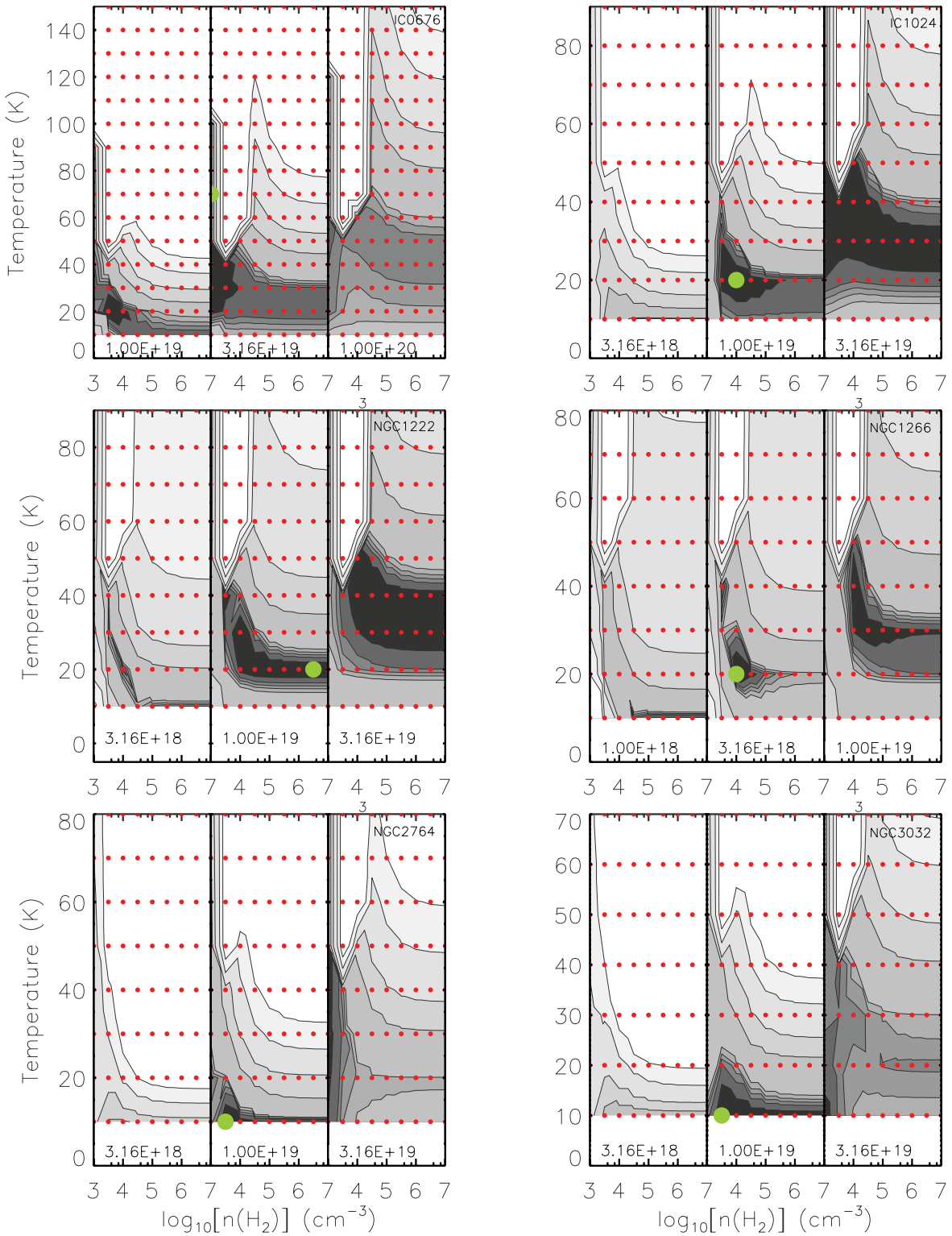

Figure 2. Best-fitting models for the CO gas component. Each panel shows the $\Delta\chi^2 \equiv \chi^2 - \chi^2_{\rm min}$ contours of the CO gas component as a function of the kinetic temperature $T_{\rm K}$ and H_2 volume density $n(H_2)$, for three values of the CO column density N(CO) (hence three plots) centred on the best-fitting value and indicated at the bottom of each plot. The model grid is shown with dark grey dots (red dots in the online version), whereas the best-fitting model of each galaxy ($\chi^2_{\rm min}$ or $\Delta\chi^2 = 0$) is labelled with a light grey filled circle (green filled circle in the online version). The $\Delta\chi^2$ contours and grey-scales are for 1–5σ confidence levels (i.e. $\Delta\chi^2 = 3.54, 6.25, 7.81, 9.35$ and 11.34 when three line ratios are used and $\Delta\chi^2 = 4.73, 7.78, 9.49, 11.14$ and 13.27 when four line ratios are used). Additional contours of $\Delta\chi^2 = 50$, 100, 200 and 300 are used in these figures only for guiding the eyes further and see better how the confidence contours are spreading within the model grid. The low σ, high confidence level contours containing 'good' models are represented by the darkest areas. The galaxy name is indicated in the top-right corner of each panel.

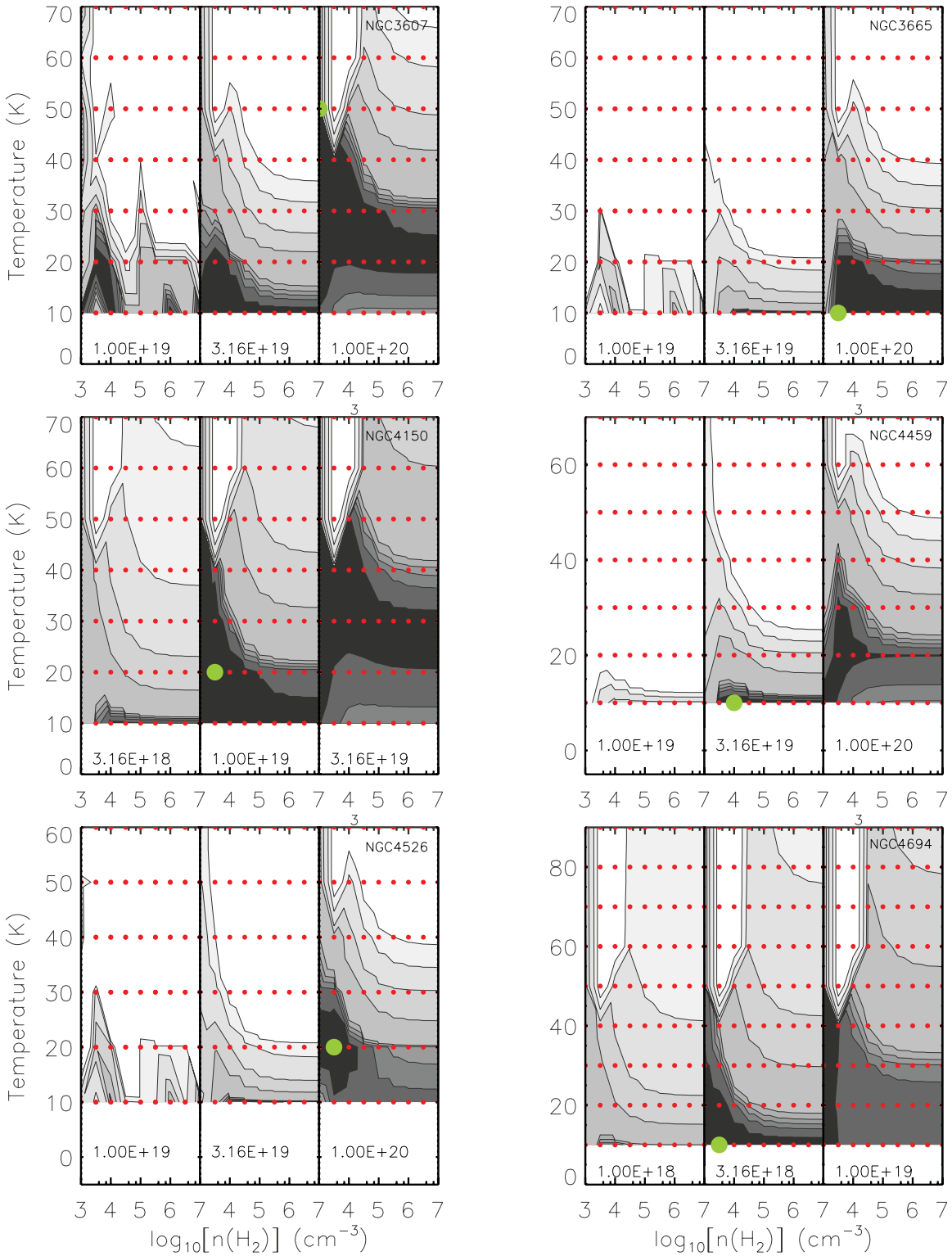

Figure 2 – *continued*

(ii) understand better the best-fitting model parameter differences across galaxies [see, e.g., Bayet et al. 2004, 2006 who used the ^{12}CO (6–5) and ^{12}CO (7–6) lines in late-type galaxies].

Despite the uniqueness of the best-fitting model for each galaxy (light grey filled circles in Fig. 2, green filled circles in the online version), there is a range of models included in the 1σ confidence level (darkest zones in Fig. 2). These models can all also be considered as good models, and they could be used to define formal uncertainties, although these would be artificially large along the three axes simultaneously and would not convey the complex shape of the $\Delta\chi^2$ contours. Indeed, as seen in Fig. 2, the contours generally have a banana-like shape similar to what is often obtained in

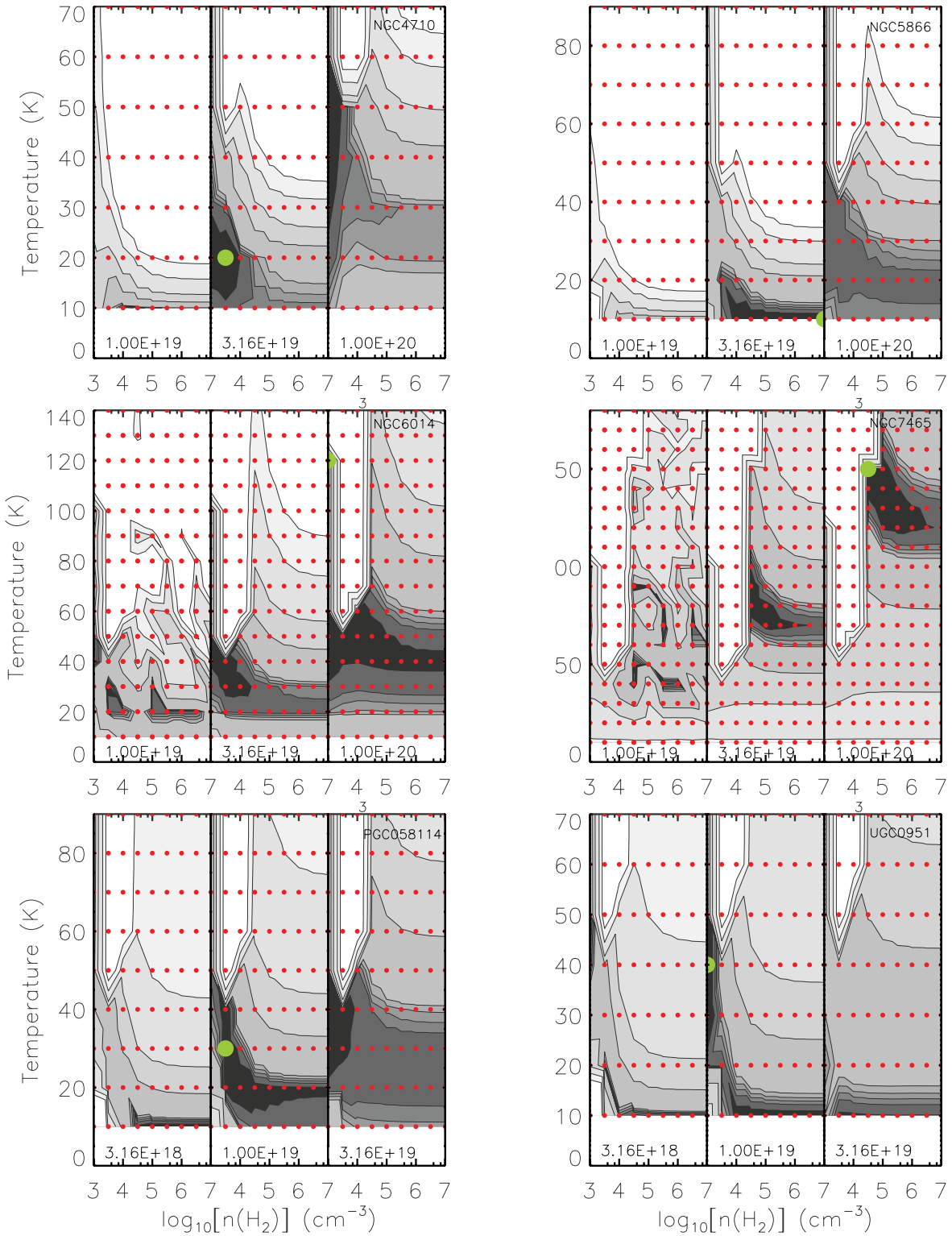

Figure 2 – *continued*

disc galaxies (e.g. Bayet et al. 2006), even if the contours are often more ragged (explained by the fact that there are fewer constraints in our study). This means that the kinetic temperature and gas volume density solutions are degenerate. Despite this, we note that the low σ confidence level contours are relatively narrow in the 3D parameter space for IC 0676, NGC 3032, NGC 4526, NGC 5866 and UGC 09519. The uncertainties on the best-fitting parameters [T_K, $n(H_2)$, $N(CO)$] are thus relatively small and the best-fitting models identified are more reliable for these sources.

4.2 Most likely model identification

To better understand the distribution of good models in our 3D parameter space, and to define robust uncertainties, we have

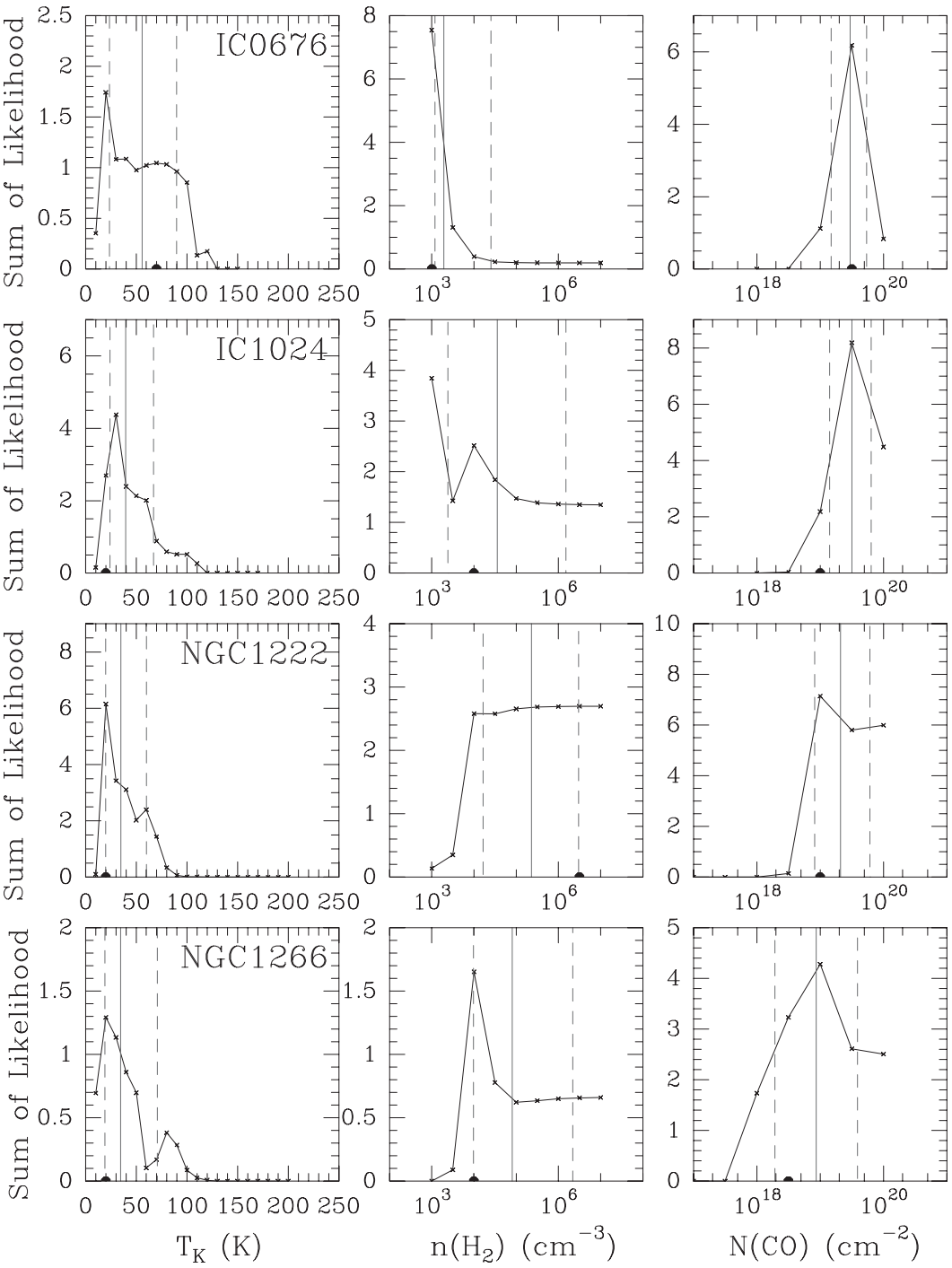

Figure 3. Marginalized PDFs of our model parameters. For each galaxy (indicated in the top-right corner of the left-hand plots), the PDF of each model parameter is shown, marginalized over the two others. The best-fitting ($\chi^2_{\rm min}$) model parameters are indicated by solid black circles on the x axes. The mean likelihood values and 1σ uncertainties are represented by solid and dashed grey lines, respectively.

investigated a complementary 'best' model identification method that consists in determining the marginalized probability distribution functions (PDFs) of the three input model parameters [$T_{\rm K}$, $n(H_2)$ and N(CO)], following the formalism developed in Kaviraj et al. (2007). For each parameter value, we have calculated the likelihood, i.e. the sum of the exponentials of $-\Delta\chi^2/2$, marginalizing over the other two free parameters. This technique allows us to isolate the effect of each parameter, and the results are shown in Fig. 3.

From the plots shown in Fig. 3, we have calculated the total area defined by each PDF, terminating the integration when necessary at the end of our model grid. This area represents the total probability (100 per cent) of each parameter, from which we have determined the mean. This defines the equipartition (50–50 per cent) of the PDF and, for well-behaved (i.e. single-peaked and symmetric) PDFs, is usually considered the most natural way to identify the most likely model. The mean is shown in each plot of Fig. 3 by a solid grey line surrounded by two dashed grey lines, themselves defining the

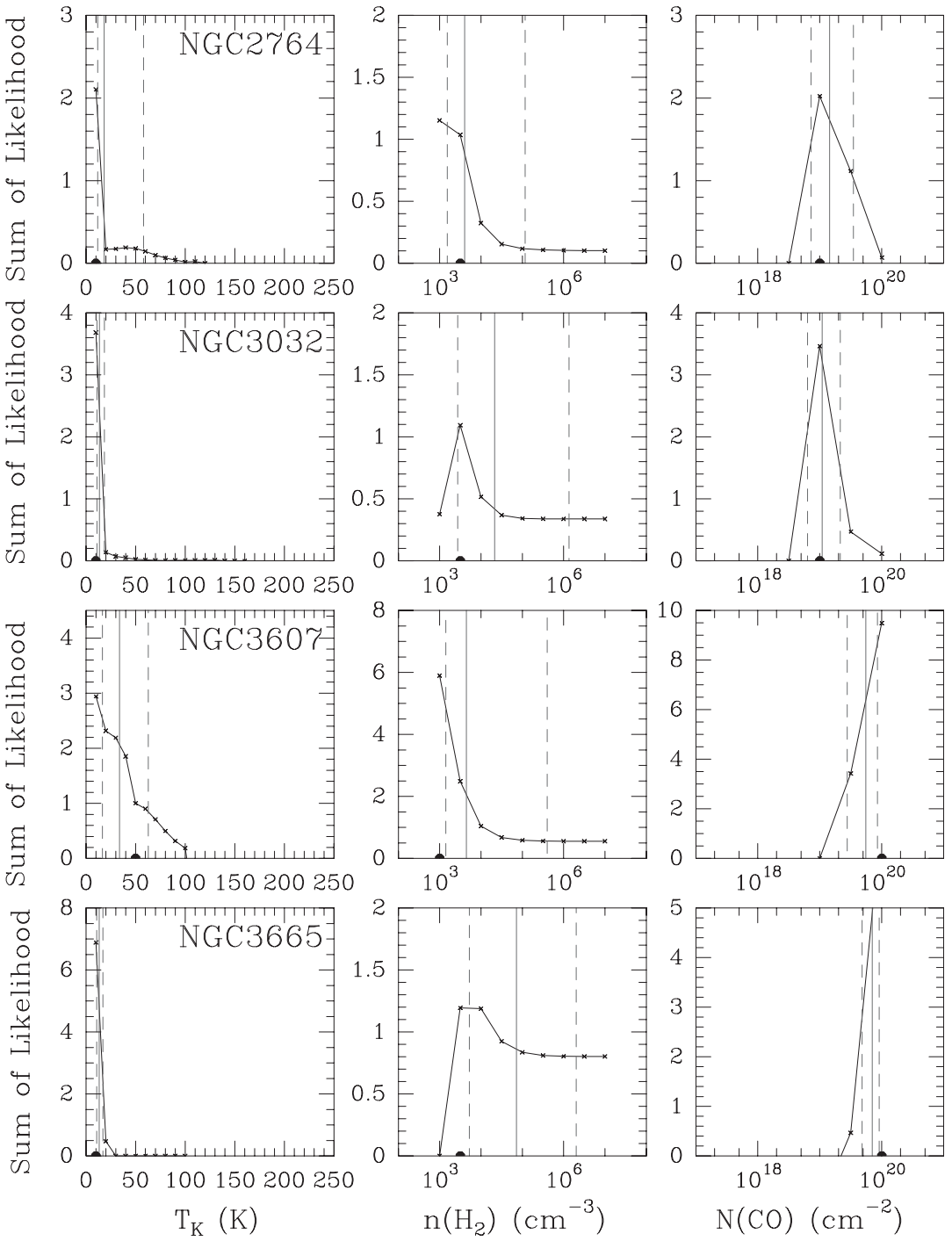

Figure 3 – *continued*

1σ uncertainty (68 per cent probability, 34 per cent on each side of the mean). The mean and associated 1σ uncertainties are listed in Table 4 for each model parameter and galaxy.

Similarly to the best-fitting method, the likelihood method yields groups of galaxies with similar ranges of kinetic temperatures. These categories are however less marked than for the best-fitting models (see Section 4.1 and Table 3). The H_2 volume densities and CO column densities are again rather uniform (variations of less than a factor of 10 for most sources, excluding NGC 1222 and NGC 5866), similar to what is observed with the best-fitting method.

The likelihood method helps us to identify the 'best' model in a complementary way to the simple χ^2 method. Comparing Tables 3 and 4 and the positions of the black dots (best-fitting models) and solid grey lines (most likely models) in Fig. 3, we see that in the majority of sources the two methods yield consistent results within the (admittedly rather large) uncertainties. Indeed, one notes that the highest PDF peaks agree well with the best-fitting model parameters. In a few cases (NGC 1266, NGC 6014 and NGC 7465 are the best examples), however, the most likely models do not exactly correspond to the best-fitting models. The apparent discrepancy between the best-fitting and most likely models is then generally due

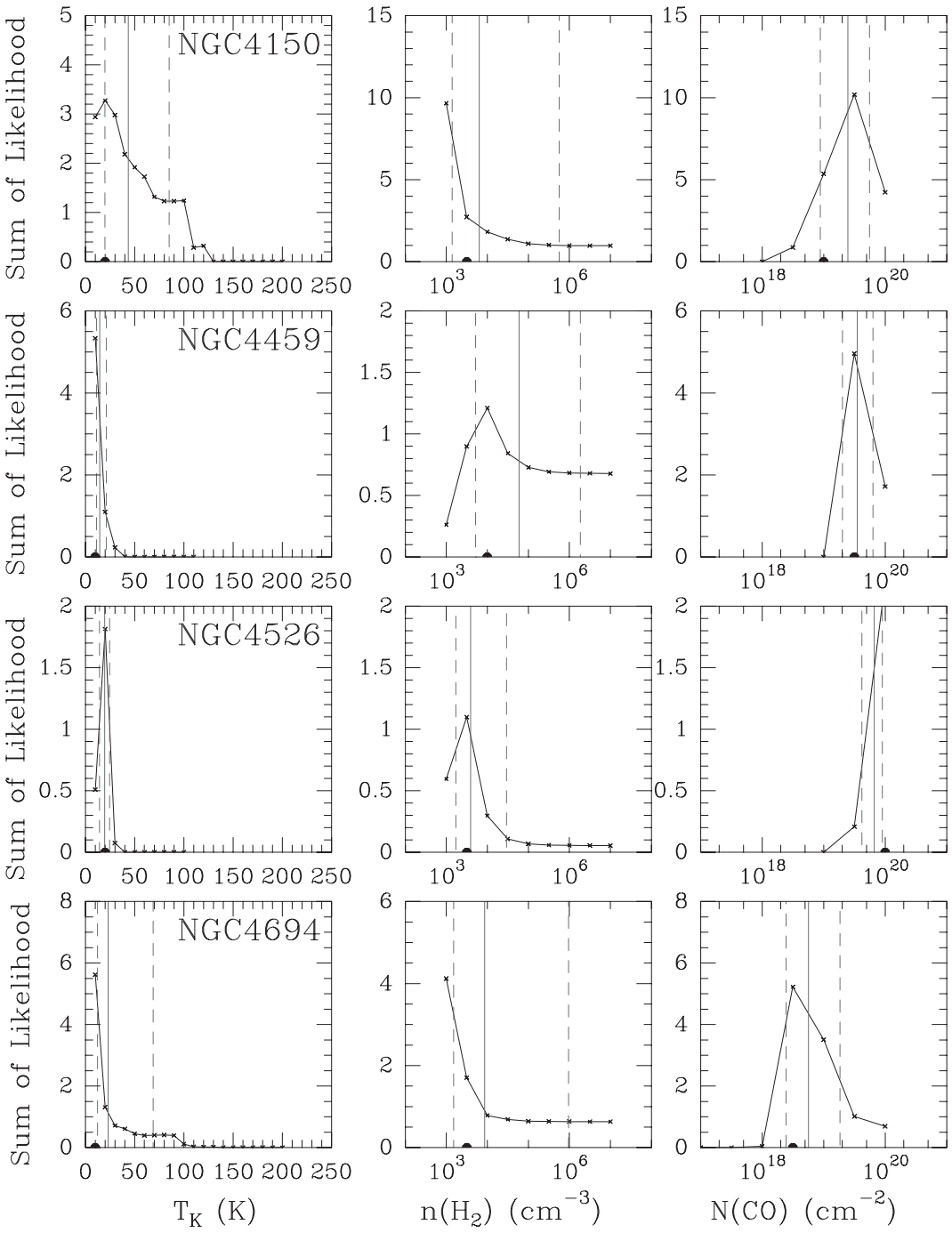

Figure 3 – *continued*

to the double-peaked (or triple-peaked for NGC 7465) shape of the kinetic temperature PDF (see the left-hand panels in Fig. 3). These two (three) peaks, when of almost equal amplitudes, imply that there are two (three) almost equally probable solutions. The derived mean for these distributions, located at a roughly equal distance from the two (three) peaks, is therefore misleading and does not generally correspond to the most likely model.

4.3 ETG CO spectral line energy distributions

Calculating models up to the 15th-level population for the CO molecule allows us to predict velocity-integrated line intensities up to ^{12}CO (15–14). Converting the velocity-integrated line intensities (in K km s^{-1}) into intensities (in W m^{-2} sr^{-1}) using equation 4 in Bayet et al. (2004), and plotting both quantities as a function of the higher rotational level of the transition considered (hereafter $J_{\rm upper}$), yields the predicted CO SLED of our ETGs (see Fig. 4).

In Fig. 4, we show the best-fitting model SLED as a solid black line and use two solid grey lines to delineate the range of SLEDs associated with a 1σ confidence level on the model parameters. In other words, all the models included within the first $\Delta\chi^2$ contour in Fig. 2 have their SLEDs between the two solid grey lines. The SLED corresponding to the most likely model is also shown as a dotted black line. Unsurprisingly, the largest 1σ SLED ranges occur

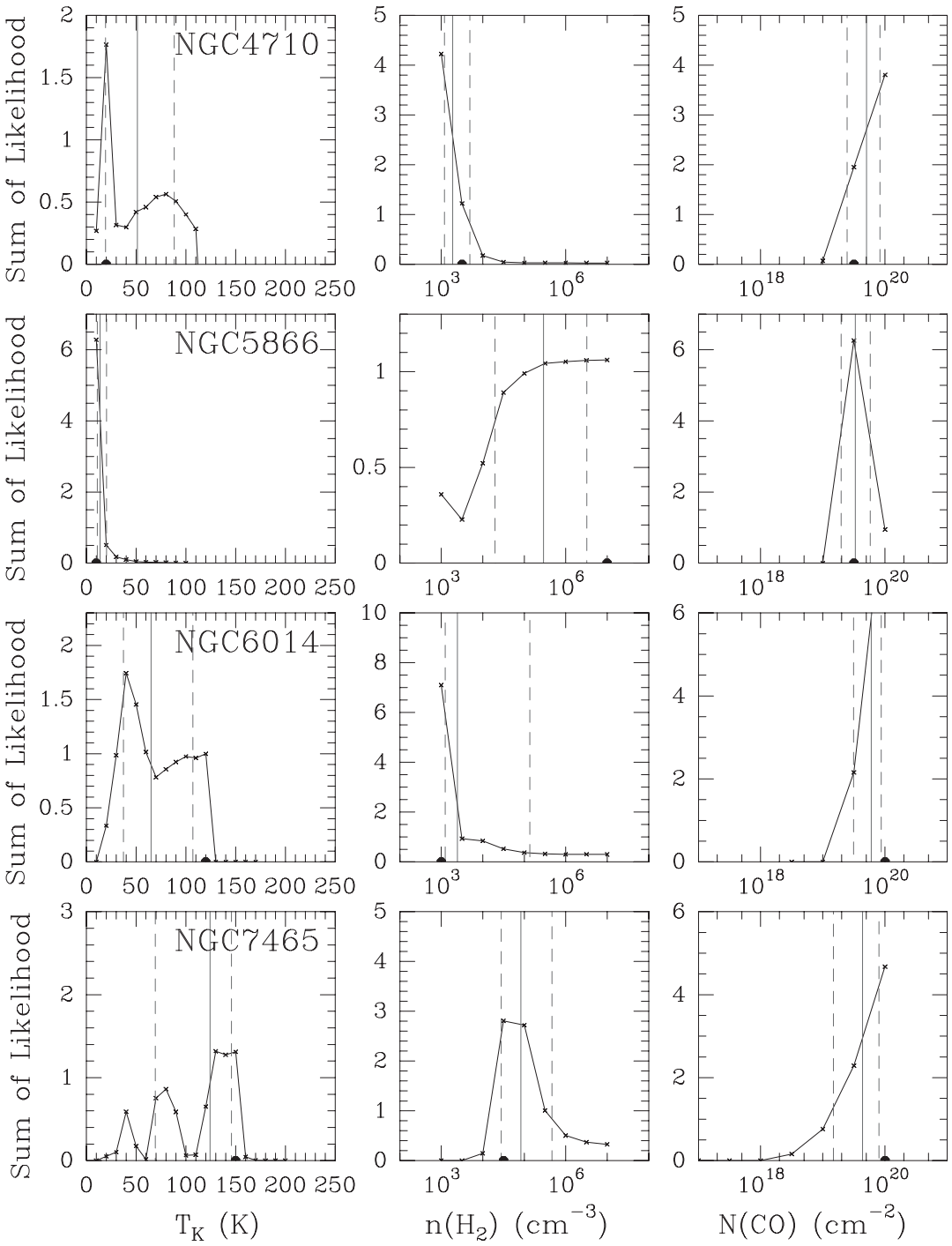

Figure 3 – *continued*

for sources with a large kinetic temperature uncertainty (i.e. when the 3D darkest region in Fig. 2 has a large extent along the *y* axis). For example, within the 1σ confidence level of its model parameters (see Fig. 2), the predicted CO SLED peak position (hereafter $J_{\rm max}$) of NGC 6014 varies between $J_{\rm upper} = 5$ and 7, covering three increments in $J_{\rm upper}$, while its kinetic temperature varies by a factor of 6. A similar behaviour is observed for NGC 1266, NGC 4694, NGC 4710, NGC 7465 and PGC 058114, with a predicted SLED turnover position increment of 2 or 3 and a kinetic temperature increase by a factor of 3–6 within 1σ. When $T_{\rm kin}$ does not vary by more than a factor of 3, $J_{\rm max}$ only varies by one increment in $J_{\rm upper}$ or less (e.g. IC 0676 and IC 1024). This provides a clear indication of how the peak of a galaxy SLED varies with kinematic temperature, and appears consistent with other current theoretical studies (e.g. Wu et al., in preparation). Of course, the H_2 volume density also has an important impact on the shape of the SLEDs, but with our present galaxy sample the corresponding effect is less clear (see Fig. 4). It is however generally thought that when the gas volume density increases, the SLED widens (Wu et al., in preparation).

To our knowledge, ours are the first CO SLEDs ever produced for normal ETGs (but see Eckart et al. 1990, Wild et al. 1997 and

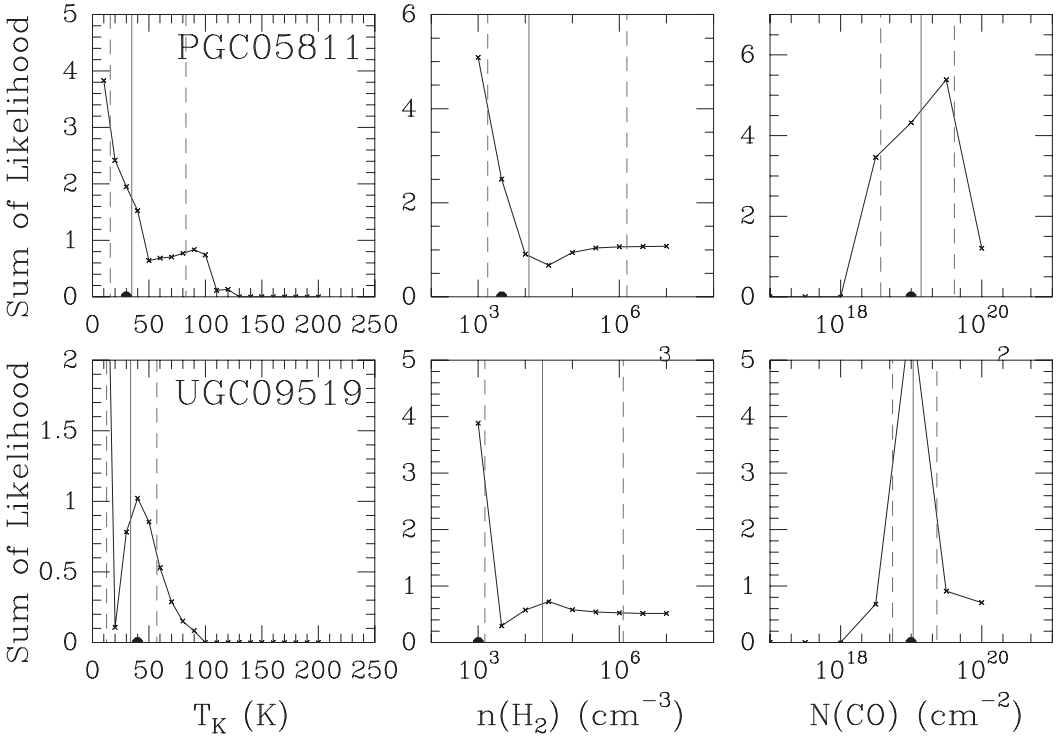

Figure 3 – *continued*

Table 4. Mean likelihood parameters and their 1σ uncertainties.

Galaxy	T_K (K)	$n(H_2)$ (cm^{-3})	$N(CO)$ (cm^{-2})
IC 0676[a]	$55.8^{+34.1}_{-32.1}$	$1.9^{+23.4}_{-0.8} \times 10^3$	$3.0^{+2.1}_{-1.5} \times 10^{19}$
IC 1024[a]	$39.6^{+27.7}_{-15.5}$	$3.6^{+147.0}_{-3.4} \times 10^4$	$3.1^{+3.2}_{-1.8} \times 10^{19}$
NGC 1222[a]	$34.8^{+25.4}_{-14.9}$	$2.3^{+27.9}_{-2.1} \times 10^5$	$2.1^{+4.0}_{-1.3} \times 10^{19}$
NGC 1266[a]	$34.7^{+36.1}_{-15.7}$	$8.1^{+211.8}_{-7.1} \times 10^4$	$8.7^{+3.0}_{-6.7} \times 10^{18}$
NGC 2764	$18.3^{+39.8}_{-6.5}$	$4.0^{+112.6}_{-2.5} \times 10^3$	$1.4^{+2.0}_{-0.7} \times 10^{19}$
NGC 3032	$13.7^{+5.1}_{-2.6}$	$2.1^{+132.3}_{-1.9} \times 10^4$	$1.1^{+1.0}_{-0.5} \times 10^{19}$
NGC 3607	$33.8^{+29.2}_{-17.1}$	$4.4^{+397.8}_{-3.0} \times 10^3$	$5.5^{+3.0}_{-2.7} \times 10^{19}$
NGC 3665	$13.4^{+3.8}_{-2.4}$	$7.2^{+195.4}_{-6.7} \times 10^4$	$7.0^{+2.0}_{-2.2} \times 10^{19}$
NGC 4150[a]	$43.6^{+41.5}_{-23.7}$	$6.3^{+563.3}_{-4.9} \times 10^3$	$2.5^{+3.1}_{-1.6} \times 10^{19}$
NGC 4459	$14.6^{+6.8}_{-3.4}$	$5.9^{+180.8}_{-5.4} \times 10^4$	$3.5^{+2.8}_{-1.5} \times 10^{19}$
NGC 4526	$19.5^{+5.0}_{-5.1}$	$3.9^{+25.4}_{-2.2} \times 10^3$	$6.7^{+2.3}_{-2.5} \times 10^{19}$
NGC 4694	$23.1^{+45.9}_{-10.6}$	$8.7^{+951.2}_{-7.2} \times 10^3$	$5.7^{+1.3}_{-3.2} \times 10^{18}$
NGC 4710[a]	$51.3^{+37.0}_{-32.0}$	$1.9^{+3.0}_{-0.7} \times 10^3$	$5.1^{+3.2}_{-2.6} \times 10^{19}$
NGC 5866	$14.0^{+6.5}_{-2.8}$	$2.9^{+29.6}_{-2.7} \times 10^5$	$3.3^{+2.4}_{-1.3} \times 10^{19}$
NGC 6014[a]	$65.1^{+42.0}_{-27.7}$	$2.5^{+135.0}_{-1.2} \times 10^3$	$6.0^{+2.7}_{-2.9} \times 10^{19}$
NGC 7465[a]	$124.3^{+21.5}_{-55.0}$	$8.3^{+38.6}_{-5.5} \times 10^4$	$4.3^{+3.6}_{-2.9} \times 10^{19}$
PGC 058114	$35.0^{+48.0}_{-19.1}$	$1.2^{+143.3}_{-1.0} \times 10^4$	$1.4^{+2.7}_{-1.1} \times 10^{19}$
UGC 09519	$33.9^{+23.2}_{-21.4}$	$2.3^{+119.1}_{-2.2} \times 10^4$	$1.1^{+1.3}_{-0.5} \times 10^{19}$

[a]Sources with a marginalized PDF with two or more peaks, where the mean parameter listed in the table is misleading, i.e. it is not the most likely parameter (see the text in Section 4.2).

Muller & Dinh-V-Trung 2009 for modelling results on Centaurus A). They are thus of prime importance to better understand the star formation activity of these systems. Indeed, J_{max} can be used as a tracer of a galaxy's star formation activity, as it is this activity that directly drives the gas excitation in most sources, including those studied here. As seen in Weiß et al. (2007) for late-type galaxies, the position of the SLED turnover appears linked to the SFR. For example, the galaxy APM 0879 (SFR $\gg 100\,M_\odot\,yr^{-1}$) has the highest observed SLED turnover position, whereas the Milky Way (SFR $\approx 1\,M_\odot\,yr^{-1}$) has the lowest. It has also been noted that the SLEDs of nearby (<10 Mpc) starburst galaxies peak at higher transitions [around (7–6)] on average than those of nearby normal spirals [such as the Milky Way, whose SLED turnover is located at around the (4–3) transition; see, e.g., Bayet et al. 2004, 2006]. Nevertheless, there is currently no study showing a direct link between a SLED turnover position and the SFR. What drives the position of the turnover is thought to be not the kinematic temperature alone, but rather a combination of the kinematic temperature and gas volume density. The gas column density is expected to impact mostly on the intensity of the SLED turnover, not its position. The $^{12}C/^{13}C$ fractional abundance (for CO), line width Δv and opacity can also influence the SLED turnover position, but they are secondary-order effects (again, see Wu et al., in preparation).

We present in Table 4 a summary of the predicted SLED turnover positions (J_{max}) for our galaxies, derived from the best-fitting models (best fit and 1σ uncertainties). We also show in Fig. 5 (top) those SLED turnover positions as a function of each of the best-fitting model parameters [T_K, $n(H_2)$ and $N(CO)$]. There are weak trends of J_{max} with both T_K and $N(CO)$. Those trends however need to be confirmed with a more reliable (i.e. larger) statistical sample, as they are mostly driven by the modelling results of a single galaxy (NGC 7465, with the highest T_{kin} and J_{max}). In addition, with only the (1–0), (2–1) and occasionally the (3–2) transition, it is often difficult to reliably predict the existence and/or position of a SLED peak, and therefore to confidently infer the level of star formation activity. The results presented here, although suggestive and exciting since available for the first time, are thus based on

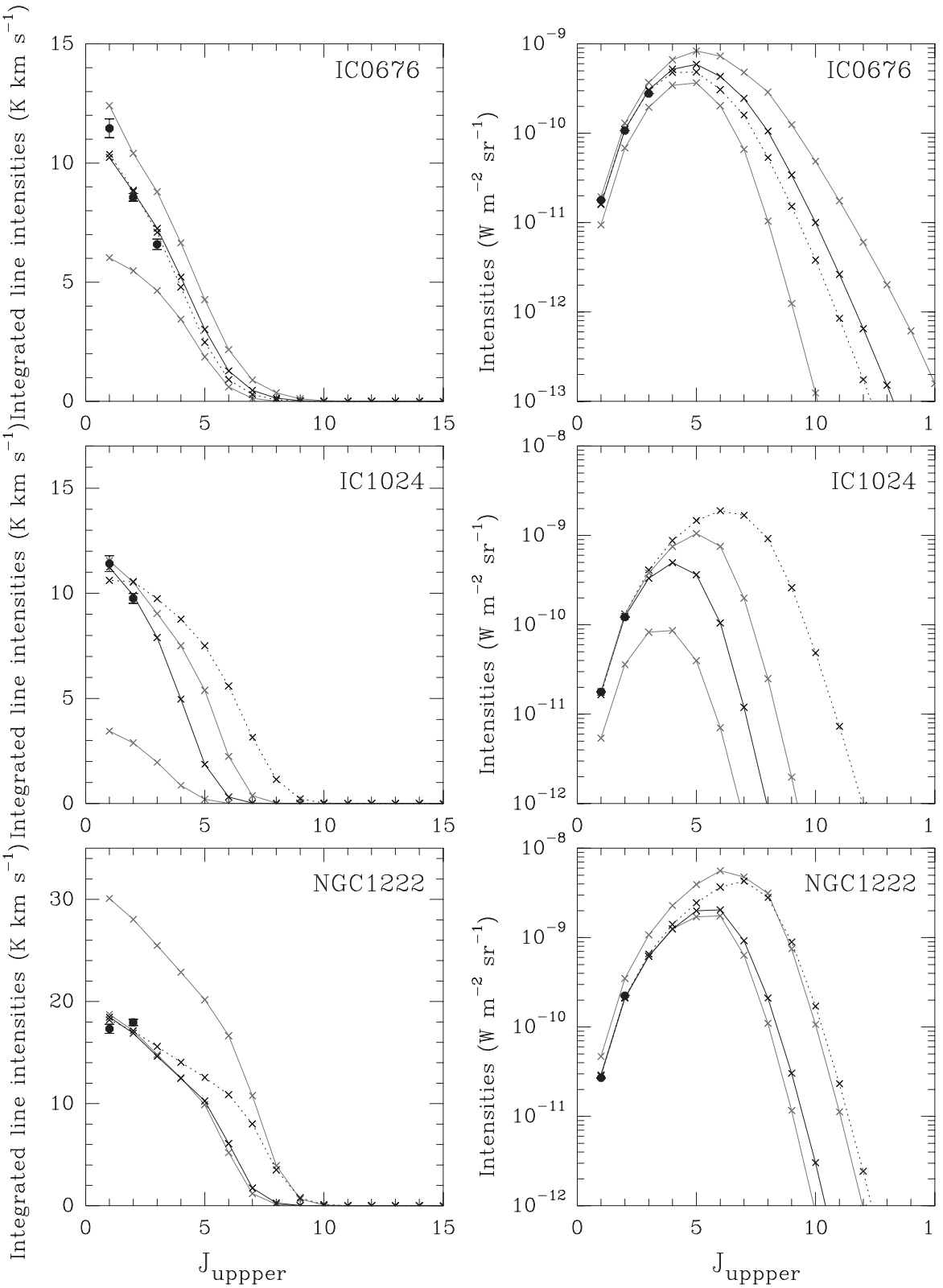

Figure 4. Predicted ^{12}CO SLEDs. For each galaxy (indicated in the top-right corner of each plot), the SLED is expressed in K km s^{-1} (left) and in W m^{-2} sr^{-1} (right). The solid and dotted black lines show the predictions from the best-fitting and most likely model, respectively. The solid grey lines define the range of possible SLEDs associated with the 1σ confidence level on the best-fitting model parameters (see Section 4.3). Crosses indicate the model predictions. The ^{12}CO observations are represented by solid black circles with error bars.

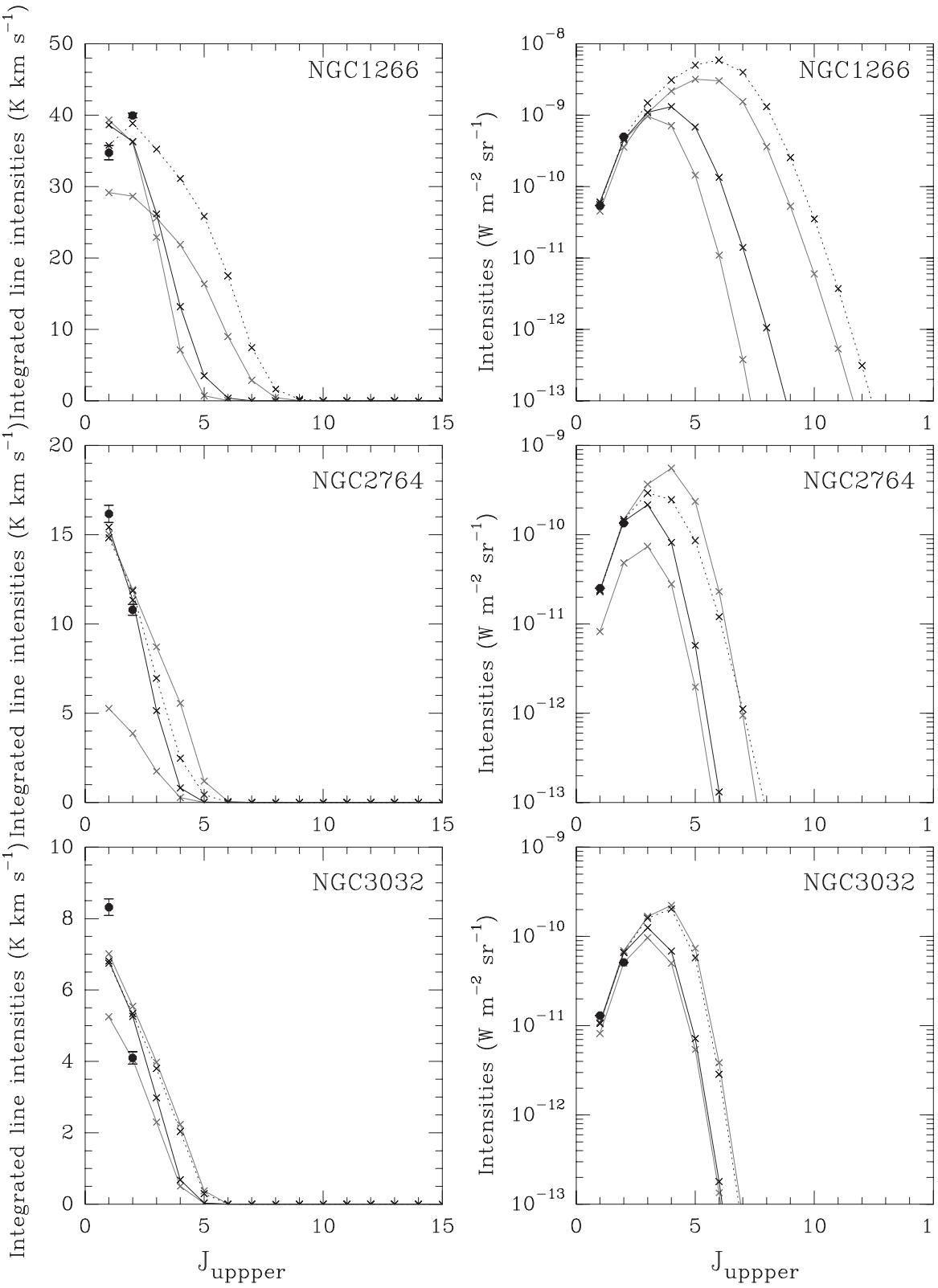

Figure 4 – *continued*

limited data and a simple theoretical model with many limitations and assumptions, and should therefore be considered accordingly.

Recently, Shapiro et al. (2010) and Falcon-Barroso et al. (in preparation) derived preliminary SFRs for eight of the molecular gas-rich ETGs in our study (NGC 1266, NGC 3032, NGC 3607, NGC 4150, NGC 4459, NGC 4526, NGC 4694 and NGC 5866), with SFRs ranging from 0.06 to 0.59 $M_{\odot}$ yr^{-1} (see Table 5). These estimates are based on non-stellar 8 μm emission. Obtaining SFR

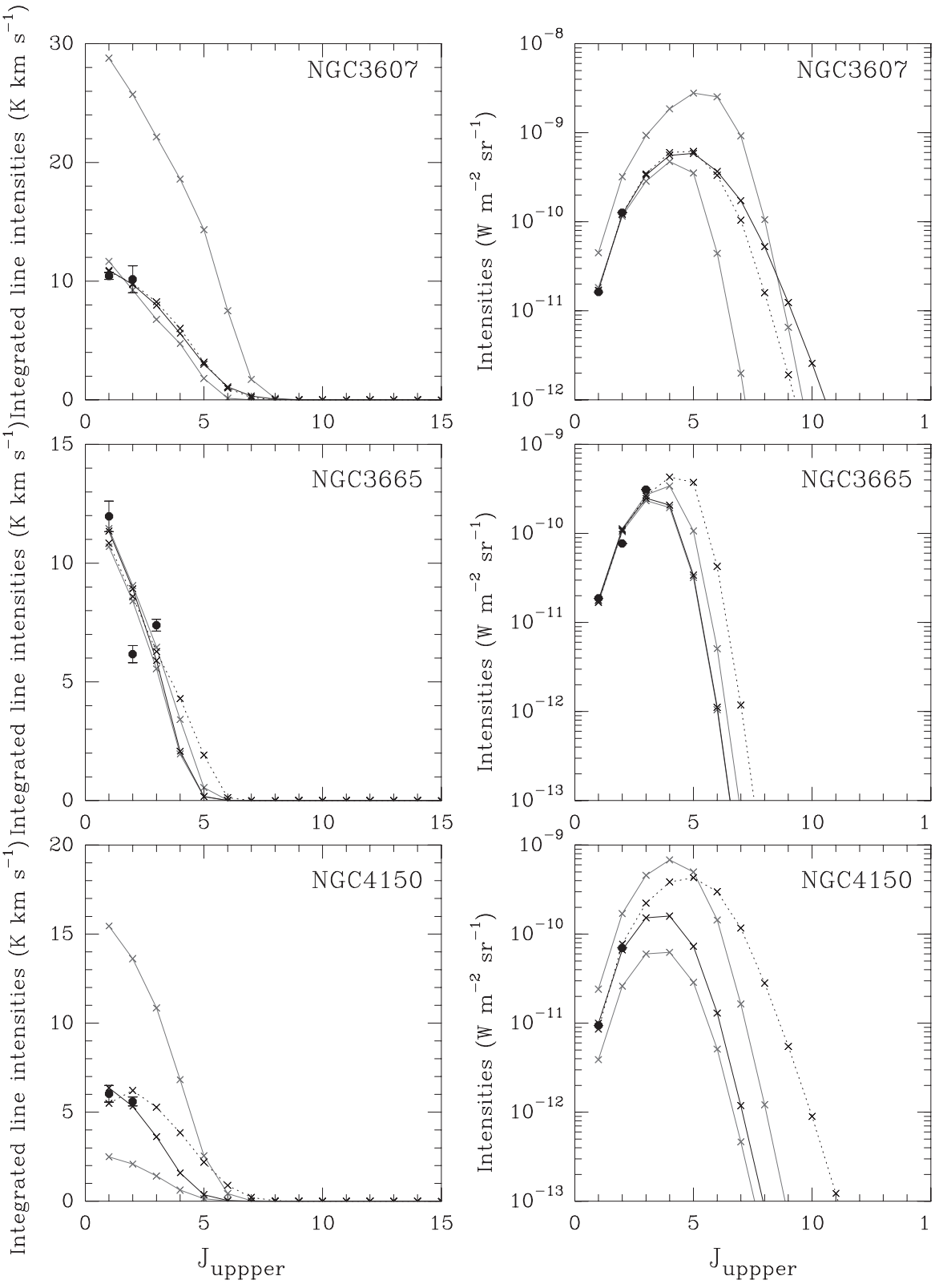

Figure 4 – *continued*

estimates for ETGs is however fraught with danger, as most usual SFR indicators are not straightforwardly applicable to ETGs. At the very least, specific properties of ETGs (e.g. UV-upturn population, X-ray haloes, etc) may significantly alter the calibration factors used in those methods (see the discussion in Crocker et al. 2011). Fig. 5 (bottom) shows the SLED turnover position as a function of the 8 μm-derived SFR for those eight galaxies. No clear trend is observed. Plots showing these SFR estimates as a function of

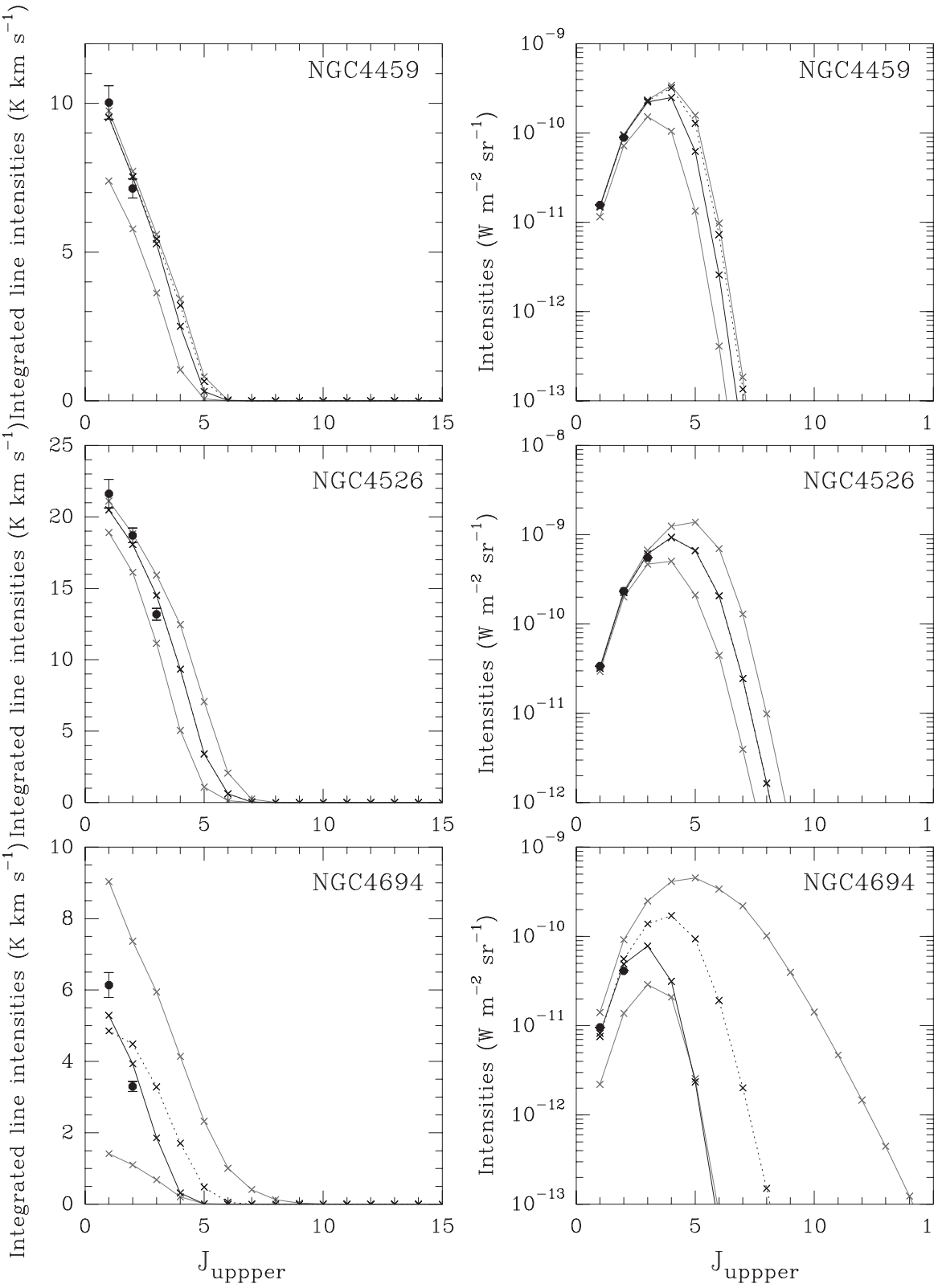

Figure 4 – *continued*

the best-fitting model parameters [T_K, $n(H_2)$ and $N(CO)$] show no clear trend either (Fig. 6). The sample size is however rather small, preventing us from drawing reliable conclusions. Whether or not ETG SLED turnover positions follow the same trend with SFR as those of late-type galaxies (e.g. Bayet et al. 2004, 2006; Weiß et al. 2007) thus remains to be confirmed. Because of the complicating issues with ETG SFRs mentioned above, a detailed study of the SFRs of our sample galaxies is beyond the scope of this paper, and

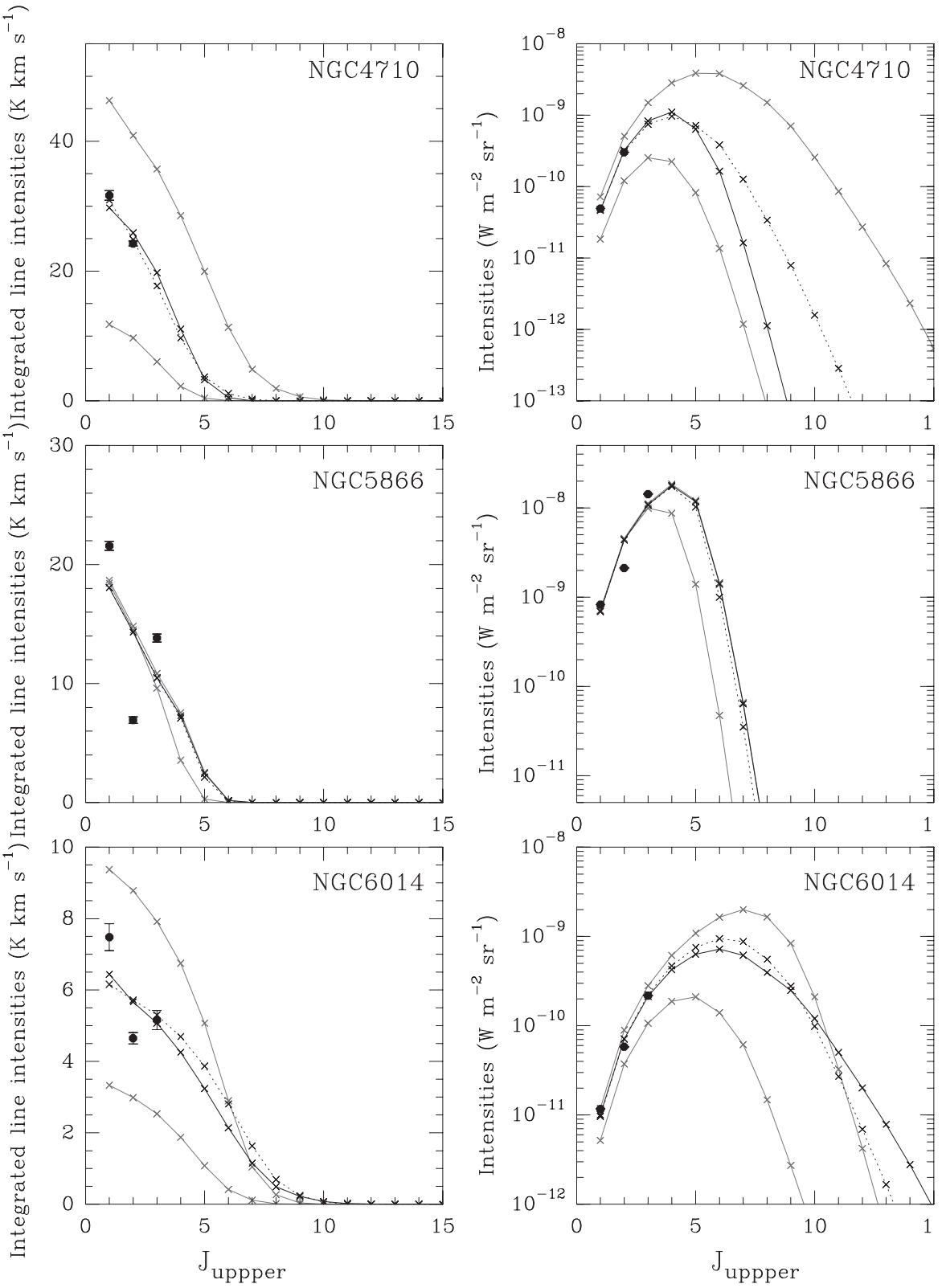

Figure 4 – *continued*

we refer the reader to Shapiro et al. (2010) and Falcon-Barroso et al. (in preparation) for further discussions.

Despite their limitations, our models are nevertheless very useful tools, making specific predictions and paving the way for future observations. These predictions can in turn inform on the models themselves. For instance, the two methods of 'best' model identification yield different predicted turnover positions in some sources. If the ^{12}CO (6–5) line was detected in IC 1024 and NGC 1266,

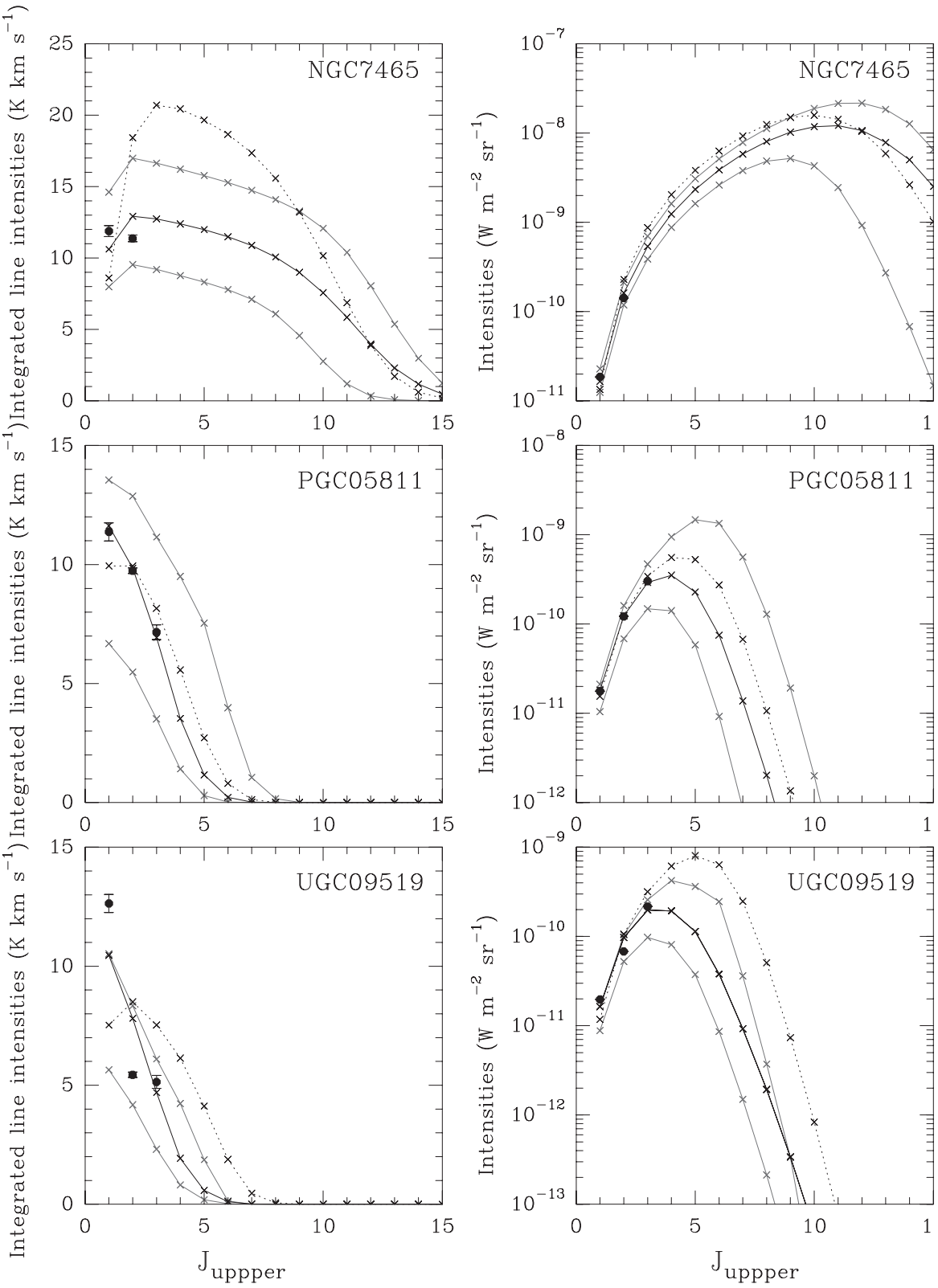

Figure 4 – *continued*

for example, with flux in both cases below 10^{-10} W m^{-2} sr^{-1}, a flat SLED seems an unlikely possibility for those two galaxies. In such case, there should rather be a SLED turnover and it should be located between $J = 2$–1 and $J = 6$–5. On the contrary, if the ^{12}CO (6–5) line was detected in these two galaxies but with a flux of about 10^{-9} W m^{-2} sr^{-1}, this will favour a flat SLED scenario thereby indicating that more sophisticated models are required to infer the properties of the molecular gas (e.g. photon-dominated

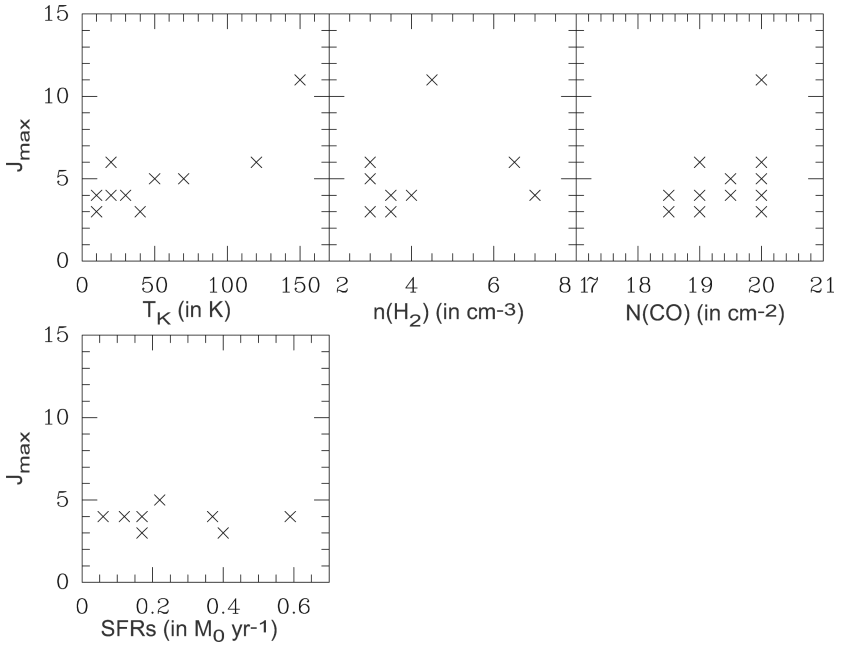

Figure 5. Top: predicted SLED turnover position (J_{max}) as a function of each of the best-fitting model parameters [T_K, $n(H_2)$ and N(CO)]. Bottom: predicted SLED turnover position (J_{max}) as a function of the 8 μm SFRs from Shapiro et al. (2010) and Falcon-Barroso et al. (in preparation), for the 8 sample galaxies where this is available (see Section 4).

Table 5. Turnover positions of the best-fitting model SLEDs.

Galaxy	J_{max}	SFR ($M_\odot$ yr^{-1})
IC 0676	5^{+0}_{-0}	
IC 1024	4^{+1}_{-0}	
NGC 1222	6^{+1}_{-0}	
NGC 1266	4^{+2}_{-1}	0.59
NGC 2764	3^{+1}_{-0}	
NGC 3032	3^{+1}_{-0}	0.40
NGC 3607	5^{+0}_{-1}	0.22
NGC 3665	3^{+1}_{-0}	
NGC 4150	4^{+0}_{-1}	0.06
NGC 4459	4^{+0}_{-1}	0.17
NGC 4526	4^{+1}_{-0}	0.37
NGC 4694	3^{+2}_{-0}	0.17
NGC 4710	4^{+2}_{-1}	
NGC 5866	4^{+0}_{-1}	0.12
NGC 6014	6^{+1}_{-1}	
NGC 7465	11^{+1}_{-2}	
PGC 058114	4^{+1}_{-1}	
UGC 09519	3^{+1}_{-0}	

Note. J_{max} uncertainties are defined as the maximum J_{max} ranges corresponding to a 1σ uncertainty on the best-fitting model parameters. SFR values are from Shapiro et al. (2010) and Falcon-Barroso et al. (in preparation).

or cosmic ray-dominated region codes such as those developed by Le Petit et al. 2006; Bayet et al. 2009b, 2011; Papadopoulos 2010; Meijerink et al. 2011). Finally, the great advantage of detecting the ^{12}CO (6–5) line, in most sources displayed in Figs 4 would be to single out the most accurate method of best model identification in ETGs (either χ^2 or maximum likelihood).

Further limits to the accuracy of the predicted SLEDs arise from the underlying assumptions that have to be carefully considered. For example, the shapes of the line profiles are neglected when working with line ratios (see Section 3.3). However, this is not true anymore when modelling velocity-integrated line intensities or intensities, and unfortunately RADEX assumes a Gaussian line profile (van der Tak et al. 2007). We know that for galaxies such as NGC 3032, NGC 3607, NGC 3665, NGC 4459, NGC 4526, NGC 5866 and NGC 6014, a double-peaked line profile is more realistic, so for these sources the SLEDs shown in Fig. 4 are more uncertain.

5 DISCUSSION

5.1 Correlations with global parameters

In Paper XI, ratios of molecular lines discussed in this paper were shown to correlate with some global physical parameters of the sample galaxies (e.g. absolute K_s-band magnitude, HI-to-H_2 mass ratio, dust morphology, etc). It is thus natural to ask if the molecular gas physical conditions derived here show similar correlations. We therefore investigated if the rough groups of sources identified in Sections 4.1 and 4.2 (see Tables 3 and 4), based on common molecular gas physical conditions, are related to other characteristics of the galaxies derived from various other ATLAS^{3D} data sets. We investigated potential correlations of our derived gas parameters with most available quantities: distance, absolute K_s-band magnitude, kinematic misalignment angle of the molecular gas with respect to the stars, inclination, HI mass, H_2 mass, 60–100 μm flux ratio (f_{60}/f_{100}), Hβ emission line equivalent width, Hβ, Mg b, Fe5015 and Fe5270$_S$ absorption line strength indices, stellar age, metallicity ([Fe/H]) and α-element (over)abundance ([α/Fe]), and effective radius (R_e). Most of these parameters were obtained from the ATLAS^{3D} survey papers (McDermid et al. 2006a,b, 2007;

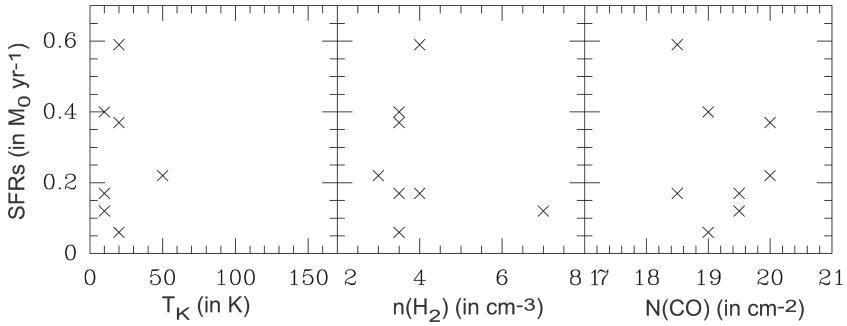

Figure 6. SFR estimates (from Shapiro et al. 2010 and Falcon-Barroso et al. in preparation) as a function of each of the best-fitting model parameters [T_K, $n(H_2)$ and $N(CO)$], for the eight sample galaxies where this is available (see Section 4).

Paper I; Paper II; Paper III; Paper IV; Davis et al. 2011b, Paper V; Paper VII; Paper X; Paper XI) or from Sarzi et al. (private communication). No correlation has been identified with any of the three model parameters [T_K, $n(H_2)$ and $N(CO)$] reproducing best the observations.

A possible explanation for the absence of any correlation is that, although the low-*J* CO transitions are good tracers of the total molecular gas reservoir, only higher *J* CO transitions closer to forming stars may correlate well with, e.g., stellar properties. Or perhaps the objects studied here simply do not span a large enough range in stellar mass. Only future observations of higher *J* CO transitions [e.g. ^{12}CO (6–5)] will confirm such a hypothesis. If a substantial fraction of the molecular gas in ETGs has an external origin, as argued in Paper X, then correlations with the dominant old stellar population may in fact not be expected. Hence, the absence of correlations may simply support the case for an external gas origin. However, given the existence of correlations with the observed line ratios (Paper XI), the absence of correlations with the derived physical conditions is puzzling. It may therefore also suggest that the models considered here are too primitive and do not do justice to the likely complexity of the ISM in the sample galaxies. Multicomponent models mixing photon-dominated, X-ray-dominated and cosmic ray-dominated regions will be investigating soon.

5.2 Literature comparison

To further understand the star formation activity of our molecular gas-rich ETGs, we compared their SLEDs and best-fitting model parameters to those obtained for well-known nearby galaxies (<10 Mpc), including starbursts (Maffei 2, a young starburst; NGC 253, an intermediate-stage starburst and M82, a post-starburst), a cosmic ray-dominated galaxy (NGC 6946), AGN-dominated galaxies (Markarian 231 and Arp 220) and normal spiral galaxies like the Milky Way. This small sample of nearby galaxies is not exhaustive, but it rather aims to be representative of the various types of star formation activity present locally. We can thus attempt to assess whether the processes at work in these well-known 'archetypes' of each star-forming class are the same (or give rise to the same gas excitation conditions) as those in ETGs. We know that the formation and evolution of ETGs and late-type galaxies are very different, but are these differences also reflected in the star-forming gas (also confined to a disc in the majority of our sample galaxies; e.g. Paper XIV; Paper XVIII)? Only a rough comparison is possible here because of the quality and incompleteness of the data sets available in the literature, but it is a useful first step.

To reproduce the low-*J* CO line emission of the young starburst galaxy Maffei 2, a kinetic temperature $T_K > 50$ K, an H_2 volume density $n(H_2) \sim 10^{3.5}$ cm^{-3} and a CO column density $N(CO) \approx 5$–7×10^{16} cm^{-2} are required (Weliachew, Casoli & Combes 1988; Hurt et al. 1993; Dumke et al. 2001). A prediction of the CO SLED turnover position is not available in the literature. Bayet et al. (2004) showed that the CO SLED of NGC 253, at an intermediate starburst evolution stage, peaks at ^{12}CO (6–5), whereas their best-fitting model parameters are $T_K = 70$–150 K, $n(H_2) \gtrsim 1 \times 10^4$ cm^{-3} and $N(CO)=1.5 \pm 0.5 \times 10^{19}$ cm^{-2}. Recent *Herschel* Observatory results on M82, a post-starburst galaxy, show that the CO SLED peaks at ^{12}CO (7–6) and that $T_K = 350$–825 K, $n(H_2) = 10^{3-4.1}$ cm^{-3} and $N(CO)=10^{18.5-19.8}$ cm^{-2} are required to reproduce the observed CO data (Panuzzo et al. 2010). We note however that observations up to the ^{12}CO (13–12) transition have been obtained, and that several gas components (whose parameters range as above) are needed to reproduce the full SLED. The authors do not provide the gas parameters for each component, so only the lower values of the ranges mentioned here are appropriate for comparison with our study. Bayet et al. (2006) showed that the CO gas component in the cosmic ray-dominated galaxy NGC 6946 requires $T_K = 130$ K, $n(H_2) = 1.5 \times 10^3$ cm^{-3} and $N(CO)=4.4 \times 10^{14}$ cm^{-2} to be excited, and that its CO SLED peaks at ^{12}CO (5–4). The AGN-dominated galaxy Markarian 231 shows an unusual CO SLED (van der Werf et al. 2010), becoming flat after the ^{12}CO (6–5) transition. Several highly excited X-ray zones combined with less excited photon-dominated regions are thought to be responsible for this behaviour. This combination yields $T_K = 70$–170 K and $n(H_2) = 10^{3-5}$ cm^{-3} globally, without indicating a specific CO column density. Similarly to the case of M82, only the lower portions of these ranges are relevant here, i.e. those susceptible to reproduce the low-*J* CO transitions. Another galaxy representing well AGN-dominated star formation activity, although perhaps less exotic than Markarian 231, is Arp 220. Greve et al. (2009), without providing the CO SLED, show that the kinematic temperature ranges from 40 to 60 K and the molecular gas volume density $n(H_2) \approx 3 \times 10^2$ cm^{-3}, again without indicating a CO column density. Finally, for the centre of the Milky Way, a normal spiral galaxy, Bayet et al. (2004) and references therein showed that the CO SLED peaks at ^{12}CO (4–3), while Sanders et al. (1992) report $T_K = 15$–20 K and $n(H_2) = 10^{3-4}$ cm^{-3}, without indicating a CO column density.

Here, despite the lack of high-*J* observations to confirm the shape of our best-fitting SLEDs, but assuming that the predicted SLEDs shown in Fig. 4 (black solid lines) are reliable (see Section 4.3), we see that the predicted CO SLEDs of most of our ETGs (13/18) peak around the (3–2) or (4–3) transition. Taking into account the

best-fitting model parameters obtained, it is thus likely that most of our molecular gas-rich ETGs have similar gas excitation conditions, and have a star formation activity similar to that present in the centre of the Milky Way. IC 0676 and NGC 3607 show CO SLED turnovers located around the ^{12}CO (5–4) transition that, when also taking into account the best-fitting model parameters [T_K, $n(H_2)$ and N(CO)] for those sources, suggest a closer proximity to Maffei 2's characteristics. NGC 1222 and NGC 6014 have molecular gas and CO SLED properties closer to those of NGC 253, while NGC 7465 seems in agreement with Markarian 231. Again, however, although these results are suggestive and interesting, we must be careful to not overinterpret them as they are extrapolations from relatively low-J CO lines only. With additional higher J CO transition data, more precise comparisons and confirmation of these results will be possible.

6 CONCLUSIONS

Exploiting recently published molecular line ratios, we have modelled for the first time the CO and HCN–HCO$^+$ gas components in a sizeable sample of gas-rich ETGs (18), this using a non-LTE theoretical method (i.e. an LVG code). We have separated these two gas components as the molecules studied are known to probe different gas phases, hence a priori should trace different physical conditions. While the HCN and HCO$^+$ lines alone leave the modelling of their corresponding gas phase degenerate, we are able to properly constrain the gas kinetic temperature, H_2 volume density and CO column density of the CO gas component using the ^{12}CO (1–0, 2–1, 3–2) and ^{12}CO(1–0, 2–1) transitions.

Most galaxies in our sample have a relatively cool (10–20 K) gas, a common H_2 volume density [$n(H_2) \sim 10^{3-4}$ cm^{-3}] and an average CO column density [$N(CO) > 10^{18}$ cm^{-2}]. For the first time, we also provide the predicted CO SLEDs of these 18 ETGs, including the predicted SLED peak position. Taking into account the gas excitation conditions, derived physical properties, and the model assumptions and limitations, most of the molecular gas in our gas-rich ETGs appears to host star formation activity at a level similar to that present in the centre of the Milky Way. Since their CO SLEDs show higher excitation conditions, a few galaxies (IC 0676, NGC 1222, NGC 3607, NGC 6014 and NGC 7465) may have slightly more active star formation or additional sources of excitation (AGN-, cosmic ray-dominated regions, etc). Strong 24, 60 and 160 μm *Spitzer* fluxes in NGC 3607 (compared to average values for ETGs) seem to confirm this hypothesis (Temi, Brighenti & Mathews 2009).

The data used to constrain our models are averaged over several kiloparsecs and often over the entire galaxy. Local (sub-kpc) gas properties could thus be significantly different from the estimates presented here, and the values listed in Table 3 and 4 should be used with caution. Nevertheless, these values are the best estimates of the molecular gas properties of ETGs available, and will remain so until spatially resolved interferometric data of multiple species and transitions become available.

This is also the first time that the physical properties are derived for two separate cold gas components in ETGs. This is a huge step forward in our understanding of current (residual) star formation in these objects. Despite the large uncertainties in the results derived for the HCN and HCO$^+$ gas component, our study nevertheless clearly shows that the physical properties of this component differ from those of the CO gas component, even in ETGs. This confirms the need for a separate treatment of these two gas components, with possibly different evolutionary paths.

It is also essential to identify additional transitions of CO, HCN and HCO$^+$ likely to improve these results and better constrain the physical properties of the dense gas in ETGs in the future. We have identified here the mid-J CO transitions [e.g. ^{12}CO (6–5)] as particularly useful, with much constraining power.

ACKNOWLEDGEMENTS

The authors thank Dr S. Kaviraj for useful discussions on the likelihood method and the referee for his/her useful comments which greatly improved the paper. The authors acknowledge financial support from ESO. EB acknowledges financial support from STFC rolling grant 'Astrophysics at Oxford 2010-2015' (ST/H002456/1) and John Fell OUP Research Fund 'Molecules in galaxies: securing Oxford's position in the ALMA era (092/267)'. TAD acknowledges funding from the European Community's Seventh Framework Programme (/FP7/2007-2013/) under grant agreement No. 229517. LMY acknowledges financial support from NSF grant 1109803. MB and TN acknowledge support from the DFG Cluster of Excellence 'Origin and Structure of the Universe'. MB has received, during this research, funding from the European Research Council under the Advanced Grant Program Num 267399-Momentum. MC acknowledges support from a Royal Society University Research Fellowship. RLD acknowledges travel and computer grants from Christ Church, Oxford and support from the Royal Society in the form of a Wolfson Merit Award 502011.K502/jd. RLD also acknowledges the support of the ESO Visitor Programme which funded a 3 month stay in 2010. SK acknowledges support from the Royal Society Joint Projects Grant JP0869822. RMM is supported by the Gemini Observatory, which is operated by the Association of Universities for Research in Astronomy, Inc., on behalf of the international Gemini partnership of Argentina, Australia, Brazil, Canada, Chile, the UK and the USA. MS acknowledges support from a STFC Advanced Fellowship ST/F009186/1. Ps is a NWO/Veni Fellow.

REFERENCES

Aladro R., Martin-Pintado J., Martin S., Mauersberger R., Bayet E., 2011, A&A, 525, 89
Alatalo K. et al., 2013, MNRAS, 432, 1796 (Paper XVIII)
Bacon R. et al., 2001, MNRAS, 326, 23
Bayet E., Gerin M., Phillips T. G., Contursi A., 2004, A&A, 427, 45
Bayet E., Gerin M., Phillips T. G., Contursi A., 2006, A&A, 460, 467
Bayet E., Lintott C., Viti S., Martín-Pintado J., Martín S., Williams D. A., Rawlings J. M. C., 2008a, ApJ, 685, L35
Bayet E., Viti S., Williams D. A., Rawlings J. M. C., 2008b, ApJ, 676, 978
Bayet E., Aladro R., Martín S., Viti S., Martín-Pintado J., 2009a, ApJ, 707, 126
Bayet E., Viti S., Williams D. A., Rawlings J. M. C., Bell T., 2009b, ApJ, 696, 1466
Bayet E., Williams D. A., Hartquist T. W., Viti S., 2011, MNRAS, 639
Bayet E., Davis T. A., Bell T. A., Viti S., 2012, MNRAS, 424, 2646
Bois M. et al., 2010, MNRAS, 406, 2405
Bois M. et al., 2011, MNRAS, 416, 1654
Bureau M. et al., 2011, MNRAS, 414, 1887
Cappellari M. et al., 2011a, MNRAS, 413, 813 (Paper I)
Cappellari M. et al., 2011b, MNRAS, 416, 1680 (Paper VII)
Combes F., Young L. M., Bureau M., 2007, MNRAS, 377, 1795
Crocker A. F., Bureau M., Young L. M., Combes F., 2011, MNRAS, 410, 1197
Crocker A. et al., 2012, MNRAS, 421, 1298 (Paper XI)
Davis T. A. et al., 2011a, MNRAS, 417, 882 (Paper X)
Davis T. A. et al., 2011b, MNRAS, 414, 968 (Paper V)

de Zeeuw P. T. et al., 2002, MNRAS, 329, 513
Dumke M., Nieten C., Thuma G., Wielebinski R., Walsh W., 2001, A&A, 373, 853
Ebneter K., Balick B., 1983, PASP, 95, 675
Eckart A., Cameron M., Genzel R., Jackson J. M., Rothermel H., Stutzki J., Rydbeck G., Wiklind T., 1990, ApJ, 365, 522
Emsellem E. et al., 2011, MNRAS, 414, 888 (Paper III)
Gao Y., Solomon P. M., 2004, ApJS, 152, 63
García-Burillo S. et al., 2006, ApJ, 645, L17
Greve T. R., Papadopoulos P. P., Gao Y., Radford S. J. E., 2009, ApJ, 692, 1432
Hurt R. L., Turner J. L., Ho P. T. P., Martin R. N., 1993, ApJ, 404, 602
Israel F. P., Baas F., 2003, A&A, 404, 495
Jeong H. et al., 2012, MNRAS, 423, 1921
Kaviraj S., Rey S.-C., Rich R. M., Yoon S.-J., Yi S. K., 2007, MNRAS, 381, L74
Kenney J. D., Young J. S., 1986, ApJ, 301, L13
Khochfar S. et al., 2011, MNRAS, 417, 845
Knapp G. R., Rupen M. P., 1996, ApJ, 460, 271
Knapp G. R., Turner E. L., Cunniffe P. E., 1985, Aj, 90, 454
Krajnović D. et al., 2011, MNRAS, 414, 2923 (Paper II)
Kramer C., Mookerjea B., Bayet E., Garcia-Burillo S., Gerin M., Israel F. P., Stutzki J., Wouterloot J. G. A., 2005, A&A, 441, 961
Krips M., Crocker A. F., Bureau M., Combes F., Young L. M., 2010, MNRAS, 407, 2261
Le Petit F., Nehmé C., Le Bourlot J., Roueff E., 2006, ApJS, 164, 506
Liszt H., 2001, A&A, 371, 865
Martig M., Bournaud F., Teyssier R., Dekel A., 2009, ApJ, 707, 250
Martín S., Aladro R., Martín-Pintado J., Mauersberger R., 2010, A&A, 522, A62
McDermid R. M. et al., 2006a, New Astron. Rev., 49, 521
McDermid R. M. et al., 2006b, MNRAS, 373, 906
McDermid R. M. et al., 2007, New Astron. Rev., 51, 13
Meijerink R., Spaans M., Israel F. P., 2007, A&A, 461, 793
Meijerink R., Spaans M., Loenen A. F., van der Werf P. P., 2011, A&A, 525, 119
Morganti R. et al., 2006, MNRAS, 371, 157
Muller S., Dinh-V-Trung, 2009, ApJ, 696, 176
Müller H. S. P., Schlöder F., Stutzki J., Winnewisser G., 2005, J. Mol. Struct., 742, 215
Müller H. S. P., Thorwirth S., Roth D. A., Winnewisser G., 2001, A&A, 370, L49
O'Connell R. W., 1999, ARA&A, 37, 603
Oosterloo T. et al., 2010, MNRAS, 409, 500
Osterbrock D. E., 1974, Astrophysics of Gaseous Nebulae. W.H. Freeman, San Francisco
Panuzzo P. et al., 2010, A&A, 518, L37
Papadopoulos P. P., 2010, ApJ, 720, 226
Roberts H., van der Tak F. F. S., Fuller G. A., Plume R., Bayet E., 2011, A&A, 525, 107
Sage L. J., Welch G. A., 2006, ApJ, 644, 850
Sage L. J., Welch G. A., Young L. M., 2007, ApJ, 657, 232
Sanders D. B., Tilanus R. P. J., Scoville N. Z., Wang Z., Zhou S., 1992, BAAS, 24, 1261
Schöier F. L., van der Tak F. F. S., van Dishoeck E. F., Black J. H., 2005, A&A, 432, 369
Serra P. et al., 2012, MNRAS, 422, 1835
Shapiro K. L. et al., 2010, MNRAS, 402, 2140
Spaans M., Meijerink R., 2005, Ap&SS, 295, 239
Temi P., Brighenti F., Mathews W. G., 2009, ApJ, 707, 890
van der Tak F. F. S., Black J. H., Schöier F. L., Jansen D. J., van Dishoeck E. F., 2007, A&A, 468, 627
van der Werf P. P., Isaak K. G., Meijerink R., Spaans M., Rykala A., Fulton T., 2010, A&A, 518, L42
Warren B. E. et al., 2010, ApJ, 714, 571
Weiß A., Downes D., Neri R., Walter F., Henkel C., Wilner D. J., Wagg J., Wiklind T., 2007, A&A, 467, 955
Welch G. A., Sage L. J., 2003, ApJ, 584, 260
Weliachew L., Casoli F., Combes F., 1988, A&A, 199, 29
Wild W., Eckart A., Wiklind T., 1997, A&A, 322, 419
Wilson T. L., Rood R., 1994, ARA&A, 32, 191
Young L. M. et al., 2011, MNRAS, 414, 940

APPENDIX A: RESULTS FOR THE HCN AND HCO$^+$ GAS COMPONENT

We present here the modelling results for the HCN and HCO$^+$ gas component, for the galaxies where both lines are detected. Fig. A1 shows the $\Delta\chi^2$ contours of the HCN–HCO$^+$ models, similarly to Fig. 2 for the CO gas component. Table A1 lists the best-fitting model parameters. The HCN–HCO$^+$ results show greater uncertainties as the models are underconstrained (one line ratio but three model parameters). They should thus be considered indicative only and should be used with caution.

Table A1. Best-fitting model parameters of the HCN and HCO$^+$ gas component.

Galaxy	χ^2	T_K (K)	$n(H_2)$ (cm^{-3})	N(HCN,HCO$^+$) (cm^{-2})
IC 0676	2.91×10^{-3}	140	10^6	$10^{19.5}$
NGC 1266	6.96×10^{-4}	90	$10^{6.5}$	$10^{19.5}$
NGC 2764	6.50×10^{-6}	190	10^4	10^{19}
NGC 3607	0.10	80	10^6	$10^{18.5}$
NGC 4710	4.72×10^{-2}	30	10^3	10^{20}
NGC 5866	4.64×10^{-2}	10	10^3	10^{20}
NGC 7465	3.14×10^{-5}	170	10^5	10^{16}

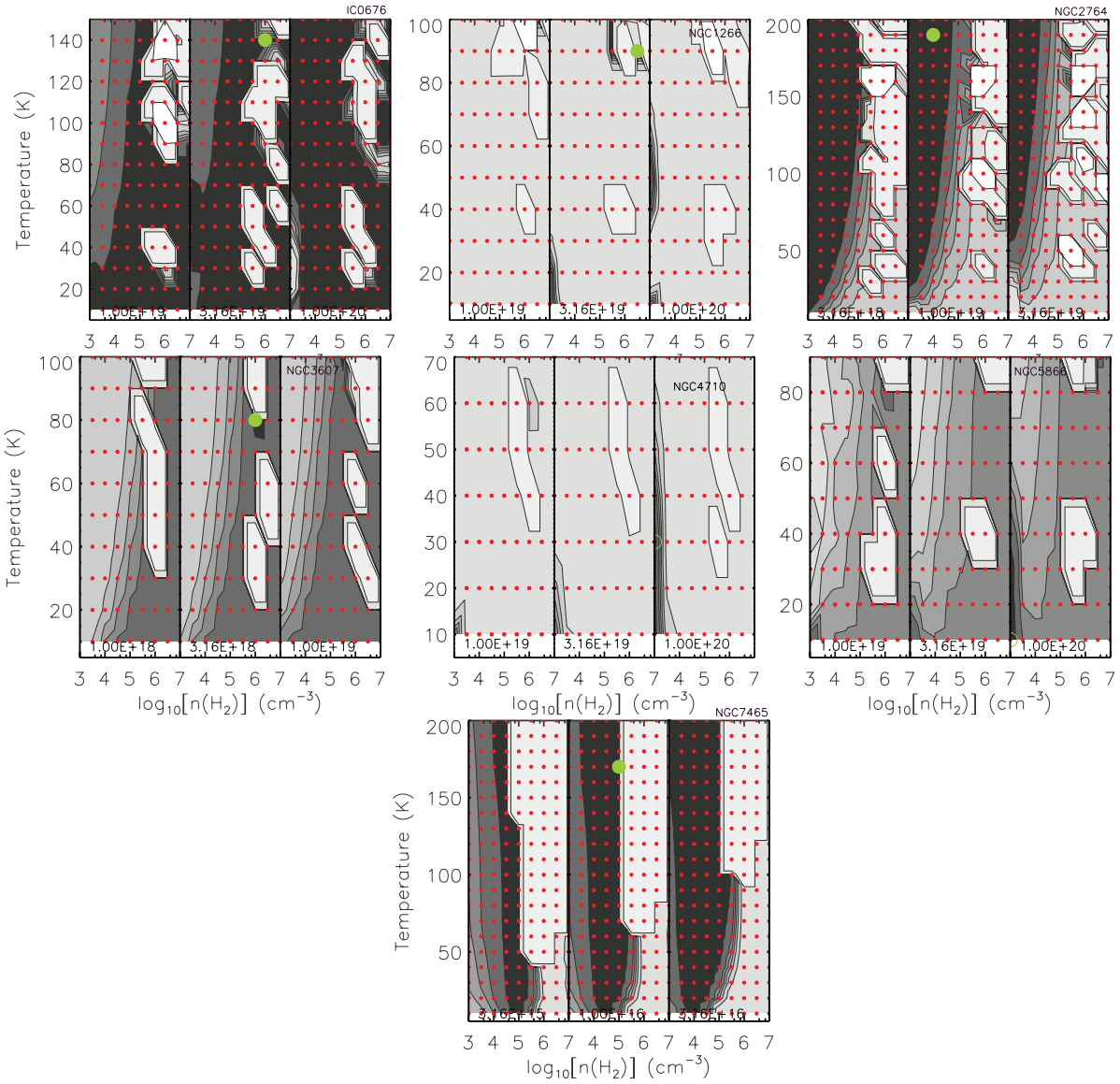

Figure A1. Best-fitting models for the HCN and HCO^+ gas component. Each panel shows the $\Delta\chi^2 \equiv \chi^2 - \chi^2_{\rm min}$ contours of the HCN and HCO^+ gas component as a function of the kinetic temperature $T_{\rm K}$ and H_2 volume density $n(H_2)$, for three values of the CO column density N(CO) (hence three plots) centred on the best-fitting value and indicated at the bottom of each plot. The model grid is shown with dark grey dots (red dots in the online version), whereas the best-fitting model of each galaxy ($\chi^2_{\rm min}$ or $\Delta\chi^2 = 0$) is labelled with a light grey filled circle (green filled circle in the online version). The $\Delta\chi^2$ contours and grey-scales are typically for 1–5σ confidence levels (i.e. $\Delta\chi^2 = 1.0$, 2.7, 3.8, 5.0 and 6.6). The low σ, high confidence level contours containing 'good' models are represented by the darkest areas. White zones correspond to models where there is no solution for fitting the single line ratio HCN (1–0)/HCO^+ (1–0). These models produce either negative opacities or negative integrated line intensities (see limitations in van der Tak et al. 2007). The galaxy name is indicated in the top-right corner of each panel.

This paper has been typeset from a TEX/LATEX file prepared by the author.